MITIGATING INTERFERENCE WITH KNOWLEDGE-AIDED SUBARRAY PATTERN SYNTHESIS AND SPACE TIME ADAPTIVE PROCESSING

THESIS

Yongjun Yoon, Capt, USAF

AFIT-ENG-MS-18-J-009

DEPARTMENT OF THE AIR FORCE
AIR UNIVERSITY

AIR FORCE INSTITUTE OF TECHNOLOGY

Wright-Patterson Air Force Base, Ohio

AFIT-ENG-MS-18-J-009

MITIGATING INTERFERENCE WITH KNOWLEDGE-AIDED SUBARRAY PATTERN SYNTHESIS AND SPACE TIME ADAPTIVE PROCESSING

THESIS

Presented to the Faculty

Department of Electrical and Computer Engineering

Graduate School of Engineering and Management

Air Force Institute of Technology

Air University

Air Education and Training Command

in Partial Fulfillment of the Requirements for the

Degree of Master of Science in Electrical Engineering

Yongjun Yoon, B.S.E.E.

Capt, USAF

June, 2018

AFIT-ENG-MS-18-J-009

MITIGATING INTERFERENCE WITH KNOWLEDGE-AIDED SUBARRAY PATTERN SYNTHESIS AND SPACE TIME ADAPTIVE PROCESSING

THESIS

Yongjun Yoon, B.S.E.E.
Capt, USAF

Committee Membership:

Lt Col Phillip Corbell, PhD
Chair

Dr. Peter J. Collins
Member

Maj James R. Lievsay, PhD
Member

AFIT-ENG-MS-18-J-009

Abstract

Phased arrays are essential to airborne ground moving target indication (GMTI), as they measure the spatial angle-of-arrival of the target, clutter, and interference signals. The spatial and Doppler (temporal) frequency is utilized by space-time adaptive processing (STAP) to separate and filter out the interference from the moving target returns. Achieving acceptable airborne GMTI performance often requires fairly large arrays, but the size, weight and power (SWAP) requirements, cost and complexity considerations often result in the use of subarrays. This yields an acceptable balance between cost and performance while lowering the system's robustness to interference. This thesis proposes the use of knowledge aided adaptive radar to institute adaptive subarray nulling in concert with digital space-time adaptive processing to improve performance in the presence of substantial interference. This research expands previous work which analyzed a clutter-free airborne moving-target indication (AMTI) application of knowledge-aided subarray pattern synthesis (KASPS) [1] and updates this previous research by applying the same concept to the GMTI application with clutter and STAP.

Acknowledgements

First and foremost, I would like to thank God for allowing me a new life and offering a sinner like me mercy, grace and love. Without you, God almighty, I could never have been here. A special thanks to my family. To my beloved wife, thank you for your sacrifice, support and love as a wife and mother of two daughters. It is a wonderful joy that our journey with God has started here at AFIT and it is such a miracle that our love has been growing with Jesus Christ. Thank you and I love you. To my parents, parents-in-law, and my sister, you flew from Korea without any hesitation to help me, I greatly appreciate your love and support. I have been deeply blessed by the kindness and caring of people I have met at AFIT and in Dayton, OH. I cannot thank them enough for what I have received and learned from these people. I would like to express my special gratitude to my advisor, Lt Col Phillip Corbell. You have been a tremendous mentor for me. You have always been there to support my research and also my family/relationship difficulties that I have been though here at AFIT. I am sincerely indebted to you for your patience, encouragement, and spiritual counseling throughout my graduate studies. Finally to all the people who encouraged me and prayed for me. I am sincerely grateful for your kindness and all your help. Thank you!

Yongjun Yoon

Table of Contents

Page

List of Figures

List of Tables

List of Abbreviations

ADBF adaptive digital beamforming

ADC analog-to-digital converter

AFIT Air Force Institute of Technology

AFRL Air Force Research Labaratory

AGL above ground level

AMF adaptive matched filter

AMTI airborne moving-target indication)

CNR clutter to noise ratio

CONOP concept of operation

CPI coherent processing interval

DARPA Defense Advanced Research Projects Agency

DOF degrees of freedom

EA electronic attack

EMI electromagnetic interference

EP electronic protection

GMTI ground moving target indication

IF improvement factor

JNR jammer-to-noise-ratio

KAPE knowledge-aided parametric covariance estimate

KA-STAP knowledge-aided space time adaptive processing

KASPS knowledge-aided subarray pattern synthesis

KASSPER knowledge-aided sensor signal processing and expert reasoning

MF matched filter

MTI moving target indication

MV minimum variance

RCS radar cross section

SBS subarray beam steering

SINR signal-to-interference and noise ratio

SNR signal-to-noise Ratio

SMF signal matched filter

STAP space-time adaptive processing.

SWAP size, weight and power

TIPD transmit interpulse pattern diversity

2D 2-dimensional

3D 3-dimensional

MITIGATING INTERFERENCE WITH KNOWLEDGE-AIDED SUBARRAY PATTERN SYNTHESIS AND SPACE TIME ADAPTIVE PROCESSING

I. Introduction

1.1 Background

Modern phased array systems are typically constrained by SWAP limitations and high cost manufacturing [2]. In order to achieve desired range and angle accuracy performance, a large aperture is usually needed. This typically requires a large number of array elements; however, the more elements the array has, the greater the cost and complexity. Ideally, every element would have its own analog-to-digital converter (ADC) in essence providing an independent receive channel for each element.

Subarraying enables the grouping of multiple elements into each channel, which reduces total number of the channels. Despite its performance tradeoffs (loss of degrees of freedom degrees of freedoms (DOFs), aliasing effects, etc), subarraying significantly saves SWAP and cost for manufacturing, test and calibration [1]. However, the decrease in DOFs results in a reduction of interference suppression performance, which is critical for electronic protection (EP) capabilities in Electronic Warfare. It is very beneficial to cancel jamming signals spatially using the phased array in order to prevent jammers from interfering with information of interest [3].

D. New's knowledge-aided subarray pattern synthesis (KASPS) algorithm improves the subarray's performance by freeing up with additional DOF by utilizing additional DOFs embedded in each subarray pattern [1]. Figure 1 shows a simplified system architecture of the KASPS. KASPS requires prior knowledge of the jammer's estimated

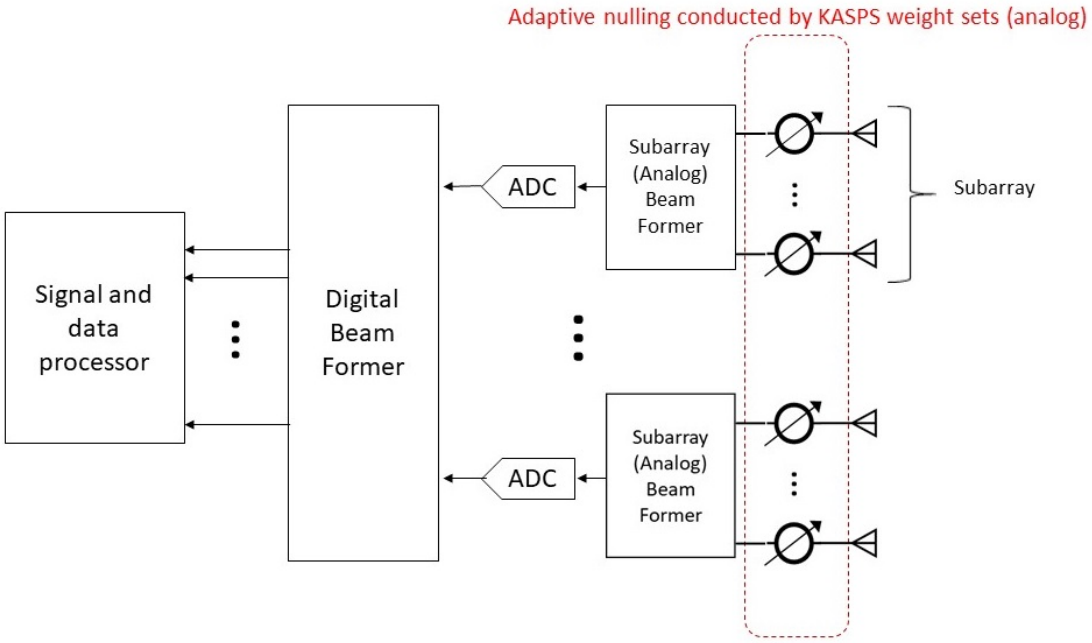

Figure 1. Structure of KASPS model

angle of arrival and jammer power information, which could be obtained from off-board intelligence or other sensors on the platform. Using this knowledge, Interference is digitally synthesized and used to generate "adaptive" digital filtering weights for each subarray using a pre-developed and calibrated look up table. The algorithm reduces the impact of grating lobes caused by subarraying and suppresses interference significantly [1].

This research investigates the implementation of the KASPS algorithm clutter. D. New's KASPS algorithm is investigated to process only spatial interference, in other words, 2-dimensional (azimuth/elevation) adaptive spatial nulling. In most of today's moving target indication (MTI) radar systems, both jammers and clutter are adaptively suppressed to improve probability of detection and reduce false alarms. The use of 2-dimensional space-time adaptive processing (STAP) with KASPS allows us to not only suppress jammers interference but also adaptively cancel clutter which spans across space and time (Doppler frequencies).

This research proposes a method to include the effects of clutter on David New's KASPS algorithm. This research evaluates the existing mathematical models that were previously used for David New's KASPS. David New used the noise, interference, and antenna model initially formulated by J. Ward in [4] and then tailored by T. Hale and Lt Col Corbell for their research provided in [5] and [6]. As with W. Melvin and G. Showman's knowledge-aided parametric covariance estimate (KAPE) method, the process envisioned here would leverage high fidelity simulated data as described in the Defense Advanced Research Projects Agency (DARPA) and As with W. Melvin and G. Showman's knowledge-aided parametric covariance estimation (KAPE) method, the process envisioned here would leverage high fidelity simulated data as described in the DARPA knowledge-aided sensor signal processing and expert reasoning (KASSPER) [7, 8]. This research also discusses a method to refine the KASPS concept of operations (CONOPs) to use a higher fidelity knowledge-aided algorithm for interference subspace prediction, generating KASPS subarray using a model based approach. This research also studies the limitations of the KASPS approach and how this addition affects various system performance metrics.

1.2 Organization

This research investigates a method to account for the clutter model with an improved version of the KASPS algorithm. Chapter 2 introduces the mathematical models of the antenna pattern, noise interference, and clutter as well as the concepts of KASPS . Chapter 3 discusses the improved KASPS algorithm to incorporate the clutter model. Chapter 4 shows the simulation results and performance analysis for various subarraying architectures facing an increasing number of jammers. Chapter 5 summarizes the findings of this research and include the suggested future work for continuing the research.

II. Background

This thesis brings together aspects of adaptive beamforming, space-time adaptive processing (STAP), phased array architecture design, knowledge-aided signal processing, and cognitive radar, each of which have a rich history. The foundations of these areas go back to the 1970's and many books have been written that survey these areas. It is beyond the scope of this thesis to review or even cite all the relevant seminal works in the literature, though key sources will be recommended from which an interested reader may get an in-depth overview on these topics. This chapter will focus on developing the mathematics and models necessary to understand the essential aspects of phased arrays, subarray manifold design, direction finding, analog (phased array) nulling, GMTI/STAP processing, broadband jamming, and knowledge-aided subarray pattern synthesis (KASPS) used in this Thesis, using references whenever possible to achieve conciseness and focus on what is new.

Adaptive antenna systems have been studied and discovered since 1950s [9]. The main definition of the term, adaptive antenna, is the adaptive nulling receive antenna system used in radar or communications [9]. The multi-channel Wiener-Hopf equation was derived by D.C. Youla in 1953, which has been a theoretical foundation of STAP technique [10, 11]. Since early 1970s, STAP methods have been vigorously adopted to null strong clutter returns for side-looking airborne radar [12]. Over the last ten years there has been rapid development in STAP technique, which allows in different directions looking array systems such as forward-looking, inclined looking, etc [12]. The concept of cognitive is a recent radar paradigm and a robust STAP technique is critical for cognitive radar to function fully adaptively [13, 14].

The first model of the digital phased array was investigated and presented in “Adaptive space-time processing techniques for airborne radars" by the Hughes Aircraft Company in 1991 [3]. The STAP was then introduced by L. Brennan with “Theory of Adap-

tive Radar." In 2002, T. Hale designed the 3D STAP technique to suppress interference in the planar array model and, then, P. Corbell developed the space time "beamforming' technique on transmit using Adaptive Illumination Patterns [1, 5, 6]. One of the most recent studies that motivated this research is D. New's knowledge-aided subarray pattern synthesis (KASPS) algorithm designed in 2015. D. New adopted the idea of Defense Advanced Research Projects Agency (DARPA)'s knowledge-aided sensor signal processing and expert reasoning (KASSPER) by utilizing T. Hale and P. Corbell's STAP models and introduced the KASPS algorithm in 2015, which optimizes the signal-to-interference and noise ratio (SINR) output performance by adaptively reducing signal return loss and suppressing interference signal sources [1]. This research introduces the background studies to understand D. New's KASPS with a 2-dimensional STAP approach.

2.1 Subarray Model

Subarraying is an affordable solution and commonly used in modern phased array systems. In non-subarrayed phased antennas, each element connects to an analog-to-digital converter (ADC) converting each element's signal to digital data for an adaptive beamforming process. A subarray, however, combines multiple elements together to function as a single element. Each of these subarrays constitutes a digitized channel. Therefore, a phased array antenna divided into multiple subarrays only requires a single ADC for each subarray, which leads to less cost and hardware complexity. The use of subarrays can potentially increase the digital degrees of freedoms (DOFs) because a subarray is formed by multiple elements and larger numbers of elements can be considered as an inherited DOFs. How many jamming signals are able to be suppressed depends on the number of DOFs so any potential improvement of the DOFs would be very beneficial if using subarrays. However, the grating lobes generated by subarray-

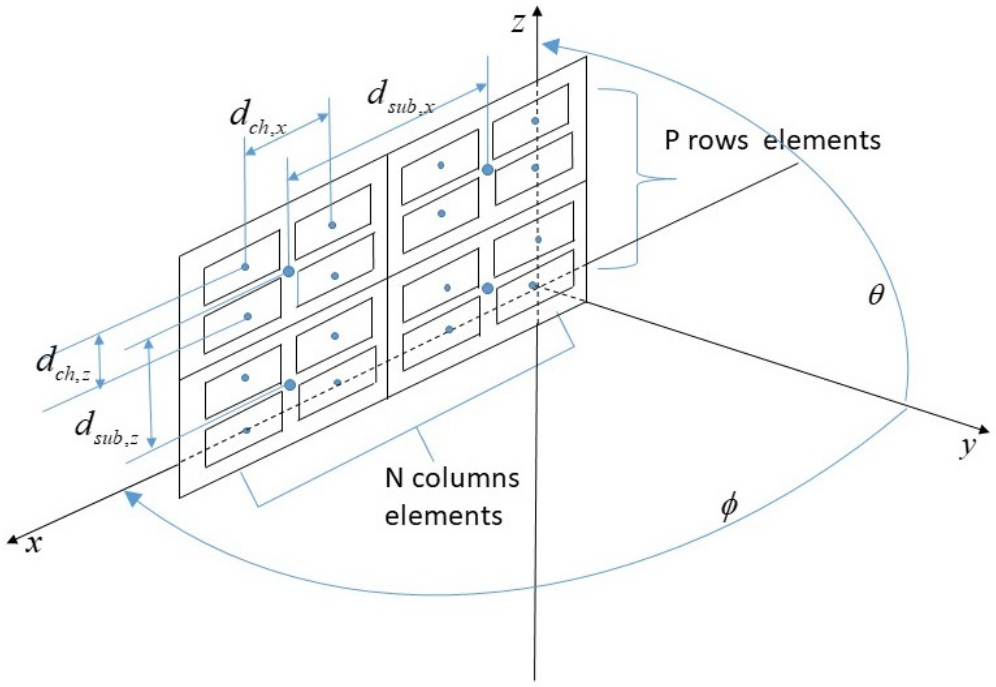

Figure 2. Geometry model of phased array [1]

ing cause ambiguities in the received pattern since the jamming signals can be copied over other spatial directions due to the appearance of multiple grating lobes' peaks and this can reduce the subarray's jammer suppression capability [1, 8]. This section documents the mathematical formulation of the subarrayed signal, noise and interference.

2.1.1 Geometry Model.

Figure 2 illustrates a typical uniform planar phased array's geometry [1]. A typical nonoverrapped planar array comprises N elements for the row and P elements for the column of the array. Grouping the whole array with multiple N_{sub} by P_{sub} array elements creates channels. This partitioning technique is called subarraying. Figure 2 shows that the 4-by-4 elements are divided into four 2-by-2 subarrays. This reduces the total number of ADCs down from 16 ADCs to 4 ADCs. The vertical and horizontal channel spacing depends upon the center frequency of the ADCs and as shown in (2),

the spacing of each element, $d_{x,elm}$ and $d_{x,elm}$ in (3), are the channel spacing. $d_{x,ch}$ and $d_{z,ch}$, are multiplied by N_{sub} and P_{sub} respectively, which shows that subarrayed channels' spacing is identified by using the distance between two adjacent subarray centers.

$$\lambda_c = c/f_c. \tag{1}$$

$$d_{x,elm} = d_{z,elm} = \lambda_c/2. \tag{2}$$

$$d_{x,ch} = N_{sub} d_{x,elm}. \tag{3}$$

$$d_{z,ch} = P_{sub} d_{z,elm}. \tag{4}$$

On the other hand, the elemental and channel spacial frequencies shown in (5) and (7) are dependent upon the antenna probing directions and channels' spacing [1].

$$\vartheta_{x,elm}(\theta_i, \phi_k) = \frac{d_{x,elm} \cos\theta_i \sin\phi_k}{\lambda_c}. \tag{5}$$

$$\vartheta_{z,elm}(\theta_i) = \frac{d_{z,elm} \sin\theta_i}{\lambda_c}. \tag{6}$$

$$\vartheta_{x,ch}(\theta_i, \phi_k) = \frac{d_{x,ch} \cos\theta_i \sin\phi_k}{\lambda_c}. \tag{7}$$

$$\vartheta_{z,ch}(\theta_i) = \frac{d_{z,ch} \sin\theta_i}{\lambda_c}. \tag{8}$$

The spatial frequencies are used to produce azimuth and elevation steering vectors for both non-subarrays and subarrays, shown in (9) and (11) [1]. These frequencies determine the number of cycles per degree for the x and z pointing direction.

$$\mathbf{a}_{ch}(\vartheta_{x,ch}) = \begin{bmatrix} 1 & e^{j2\pi\vartheta_{x,ch}} & \dots & e^{j2\pi(N-1)\vartheta_{x,ch}} \end{bmatrix}^T. \tag{9}$$

$$\mathbf{e}_{ch}(\vartheta_{z,ch}) = \begin{bmatrix} 1 & e^{j2\pi\vartheta_{z,ch}} & \dots & e^{j2\pi(P-1)\vartheta_{z,ch}} \end{bmatrix}^T. \tag{10}$$

$$\mathbf{a}_{sub}(\vartheta_{x,elm}) = \begin{bmatrix} 1 & e^{j2\pi\vartheta_{x,elm}} & \dots & e^{j2\pi(N_{sub}-1)\vartheta_{x,elm}} \end{bmatrix}^T. \tag{11}$$

$$\mathbf{e}_{sub}(\vartheta_{z,elm}) = \begin{bmatrix} 1 & e^{j2\pi\vartheta_{z,elm}} & \dots & e^{j2\pi(P_{sub}-1)\vartheta_{z,elm}} \end{bmatrix}^T. \tag{12}$$

Using the Kronecker product, shown in (13), $\otimes$, creates steering vectors considering both azimuth and elevation spatial frequencies [1].

$$\mathbf{v}_{sub}(\theta_t, \phi_t) = \mathbf{e}_{sub}(\vartheta_{z,elm}(\theta_t)) \otimes \mathbf{a}_{sub}(\vartheta_{x,elm}(\theta_t, \phi_t)). \tag{13}$$

$$\mathbf{v}_{sub} = \mathbf{e}_{sub}(\vartheta_{z,elm}(\theta_t, \phi_t)) \otimes \mathbf{I}_{\mathbf{M}} \otimes \mathbf{a}_{sub}(\vartheta_{x,elm}(\theta_t, \phi_t)). \tag{14}$$

2.2 Clutter Model

The ground moving target indication (GMTI) uses Doppler filtering to isolate a ground moving target return from unwanted large target retruns; this radar scheme has a problem because it produces sidelobe clutter across space and time. The key process for the STAP filtering is synthesizing the snapshot which represents the specific element, pulse and range gate for noise and interference including jammers and clutters for its adaptive filtering. This masks target signals and degrades target detection. One of the classical methods to solve the clutter problem is STAP-based GMTI radar. Prior to introducing the overview of the STAP process, this section discusses the traditional clutter model and how to filter it and measure its suppression performance.

2.2.1 Geometry Model of Clutter.

The geometry model of the clutter as shown in Figure 3 depicts the sequence of scanning patches rotated and elevated to (θ_i, ϕ_k). The clutter model shows a single clutter patch at least R_u away from the center point where the reference point of the array is projected to the ground in order to prevent ambiguity in signal return. θ_i is

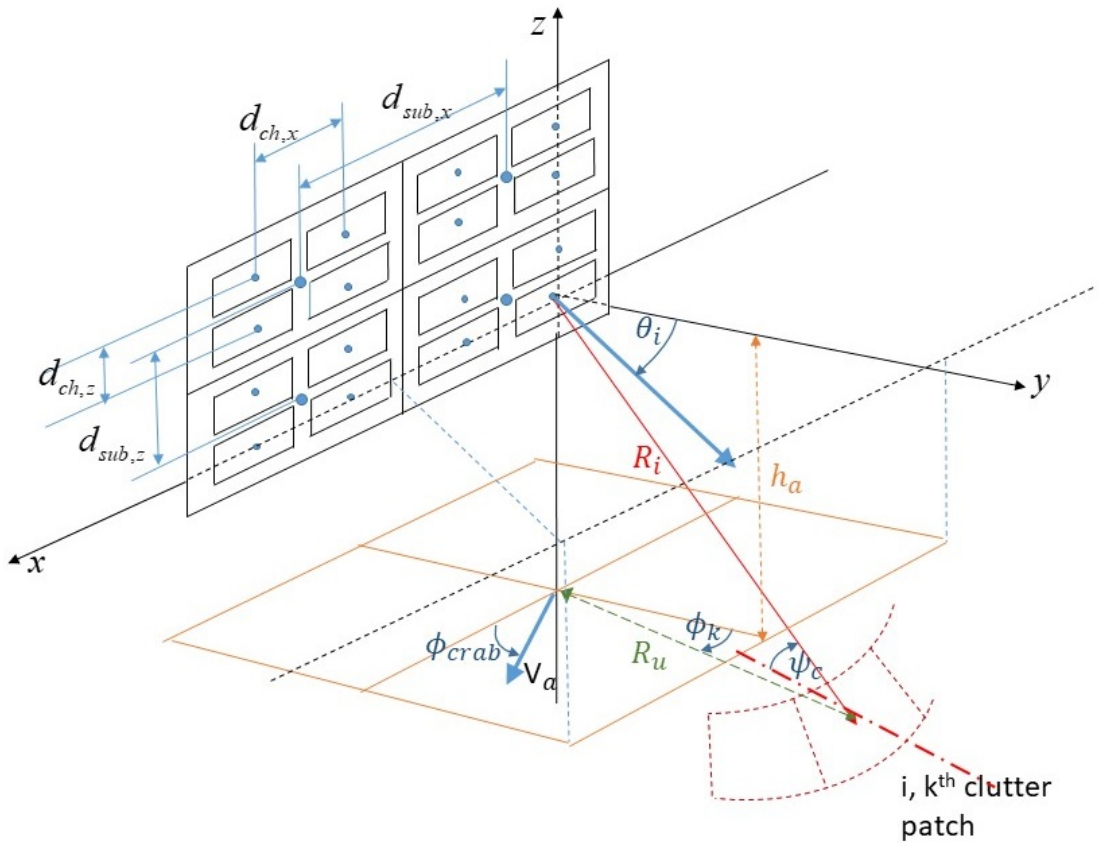

Figure 3. Geometry of clutter model

an elevation angle to a clutter patch, which is described by the (16). h_a is the above ground level (AGL). R_i is the range to the 'i' th range ring and a_e is the effective radius of the earth, typically designed as 3/4 radius. The 'k' clutter patch azimuth angle ϕ_k is given in (15)

$$\phi_k = \left\{ \frac{k2\pi}{N_c} : k = 0, 1, 2, \ldots N_c - 1 \right\}. \tag{15}$$

$$\theta_i = -\sin^{-1}\left[\frac{R_i^2 + h_a(h_a + 2a_e)}{2R_i(a_e + h_a)} \right] \tag{16}$$

$$R_h = \sqrt{h_a^2 + 2h_a a_e} \tag{17}$$

$$R_u = \frac{c\, T_{PRI}}{2}. \tag{18}$$

$$N_r = \left\lfloor \frac{R_h}{R_u} \right\rfloor. \tag{19}$$

2.2.2 Antenna Pattern.

The spatial steering vectors,$\mathbf{v}_{ch}(\theta_t,\phi_t)$ and $\mathbf{v}_{sub}(\theta_t,\phi_t)$, given in (13) steer the array factors towards the target look angle (θ_t,ϕ_t) shown in (20). The steered array factors are multipled with the received element pattern, g_{sub}, which forms the antenna pattern, (22). If the elements are not subarrayed, the received element pattern is equaled to the transmitted antenna pattern, g_{elm}, shown in (23). However, the received element pattern of the subarrayed phased array is obtained by the array factor formed from each element of its single subarray and the received pattern is given in [1], shown in (23).

$$\mathbf{AF}_{ch}(\theta,\phi)=\mathbf{w}_{ch}{}^{H}\mathbf{v}_{ch}(\theta_t,\phi_t). \tag{20}$$

$$\mathbf{AF}_{sub}(\theta,\phi)=\mathbf{w}_{sub}{}^{H}\mathbf{v}_{sub}(\theta_t,\phi_t). \tag{21}$$

$$G(\theta,\phi)=|\mathbf{AF}_{ch}(\theta,\phi)|^2 g_{sub}(\theta,\phi). \tag{22}$$

$$g_{sub}(\theta,\phi)=|\mathbf{AF}_{ch}(\theta,\phi)|^2 g_{elm}(\theta,\phi). \tag{23}$$

In this research, g_{elm} in (23) is modeled with a microstrip element model. The model is controlled with two micrstrip spacings which is very common in modern phased array applications [1]. [15] The parameter S in (24) is effectively used to manipulate the beamwidth, where S is the spacing between two slots. As in D. New's work, "S" is set such that the element pattern has a 2 dB drop in gain when steered to 60 degrees off boresight [1].

$$f(\theta,\phi)=\begin{cases} g_e \frac{\sin(S\sin\theta)\sin(S\sin\phi)}{4\sin\left(\frac{S}{2}\sin\theta\right)\sin\left(\frac{S}{2}\sin\phi\right)} & -90^\circ\geq\phi,\theta\geq 90^\circ \\ b_e g_e \frac{\sin(S\sin\theta)\sin(S\sin\phi)}{4\sin\left(\frac{S}{2}\sin\theta\right)\sin\left(\frac{S}{2}\sin\phi\right)} & 90^\circ\geq\phi,\theta\geq 270^\circ. \end{cases} \tag{24}$$

The subarray's array factor generates multiple grating lobes due to increased ele-

ment's spacing, which can be computed from (25) if meeting the condition shown in (26).

$$\left(\cos\theta_{tl}\sin\phi_{tl} \pm \frac{m\lambda_c}{d_{x,ch}}\right)^2 + \left(\sin\phi_{tl} \pm \frac{m\lambda_c}{d_{x,ch}}\right)^2 < 1 \tag{25}$$

$$\begin{aligned} &\theta_{GL} = \sin^{-1}(\sin\theta_{dl} \pm \tfrac{l\lambda_c}{d_{z,ch}}), \\ &\phi_{GL} = \sin^{-1}\left(\frac{\cos\theta_{dl}\sin\phi_{dl} \pm \frac{m\lambda_c}{d_{x,ch}}}{\cos\left(\sin^{-1}\left(\sin\phi_{dl} \pm \frac{m\lambda_c}{d_{z,ch}}\right)\right)}\right). \\ &l = 0,1,2,\ldots,\ m = 0,1,2,\ldots \end{aligned} \tag{26}$$

2.2.3 Noise Model.

$\mathbf{N}_{in,elm}$ is the input noise power per an element, which is a thermal noise as given in (27). The output noise power per each channel, therefore, is obtained by multiplying a scale factor which is the total signal power received from the weights used on elements in a subarray and multiplying the Noise Figure, F_N, which is shown in (28) channel.

$$\mathbf{N}_{in,elm} = K T_o B. \tag{27}$$

$$\mathbf{N}_{out,ch} = N_{sub} P_{sub} \mathbf{N}_{in,elm} F_N. \tag{28}$$

The noise covariance is simply formed with the channel noise power on the unit covariance in (30). The noise snapshot is formulated using the $M \times 2NMP$ sized of noise realization matrix with the complex normal distribution form, shown in (29).

$$\chi_{N,ch} \sim N\left(0, \frac{\mathbf{N}_{out,ch}}{2}\right) + iN\left(0, \frac{\mathbf{N}_{out,ch}}{2}\right). \tag{29}$$

$$\mathrm{R}_{N,ch} = E\{\chi_c {\chi_c}^H\} = \mathbf{N}_{out,ch}\mathbf{I}_{MNP}. \tag{30}$$

2.2.4 Jammer Model.

As shown in (32), the jammer-to-noise-ratio (JNR) for the subarray, ξ_{JNR}, is dependent upon the jammer parameters such as received jammer power, P_J, and jammer ranges, R_{jrng}. Also the JNR is inversely proportional with system loss, L_S, as the typical radar range equation. The received power is the product of jammer's power spectral density per hertz, J_o and its bandwidth, B, as shown in (31). Here 'n' is the 'n'th jammer when multiple jammers are present. Since the received antenna pattern is the subarray pattern and the subarray pattern's mainbeam is steered to the jammer direction, the subarray pattern gain, $g_{sub}(\theta_{J,n}, \phi_{J,n})$, changes for each look angle and JNR is diffenrent at each look angle as well.

$$P_{J,n} = J_o B. \tag{31}$$

$$\xi_{JNR,n} = \frac{g_{sub}(\theta_{J,n}, \phi_{J,n})\lambda_c^2 P_{J,n}}{(4\pi)^2 L_S {R_{jrng,n}}^2 \mathbf{N}_{out,ch}} = \frac{|\mathbf{AF}_{sub}(\theta_{J,n}, \phi_{J,n})|^2 g_{elm}(\theta_{J,n}, \phi_{J,n})\lambda_c^2 P_{J,n}}{(4\pi)^2 L_S {R_{jrng,n}}^2 \mathbf{N}_{out,ch}}. \tag{32}$$

The amplitude of the jamming snapshot is modeled as shown in (33). The amplitude is the result of multiplication of the noise model shown in 2.1.3 and the JNR using the M X 2NMP sized of random realization matrix with the complex normal distribution form. Then, the jamming snapshot in (34) is formed by summing up the steering vector that points to jammer direction multiplied by (33) for each jammer. Similarly, the Jammer covariance matrix is derived by summing the received jammer power multiplied with the Hermitian vector multiplication of the steering vector for each jammer.

$$\alpha_{J,ch,n} \sim N\left(0, \frac{\mathbf{N}_{out,ch}\xi_{JNR,n}}{2}\right) + iN\left(0, \frac{\mathbf{N}_{out,ch}\xi_{JNR,n}}{2}\right). \tag{33}$$

$$\chi_{J,ch} = \sum_{n=1}^{M} \mathbf{e}_{ch}(\vartheta_{z,ch}(\theta_t)) \otimes \alpha_{J,ch,n} \otimes \mathbf{a}_{ch}(\vartheta_{x,ch}(\theta_t, \phi_t)). \tag{34}$$

$$\mathrm{R}_{J,ch} = \sum_{n=1}^{M} E\{\chi_{J,n}{\chi_{J,n}}^{H}\} = \sum_{n=1}^{M} \mathbf{N}_{out,ch}\xi_{JNR,n}[\mathbf{e}_{ch}(\vartheta_{z,ch}(\theta_t))\{\mathbf{e}_{ch}(\vartheta_{z,ch}(\theta_t))\}^{H} \otimes \mathbf{I_M} \otimes \mathbf{a}_{ch}(\vartheta_{x,ch}(\theta_t,\phi_t))\{\mathbf{a}_{ch}(\vartheta_{x,ch}(\theta_t,\phi_t))\}^{H}] \tag{35}$$

2.2.5 Clutter Space Time Snapshot and Covariance Matrix.

The target Doppler frequency determines the speed of each scanning move and it is normalized by the pulse repetition interval (PRI), which is shown in (36).

$$\omega_{ik} = \frac{2v_a \cos(\theta_i)\sin\left(\phi_k + \phi_{crab}\right)}{\lambda_c f_{PRF}} = \beta\vartheta_{x,ch}(\theta_i, \phi_k + \phi_{crab}). \tag{36}$$

By applying the Doppler dependency into the steering vector used in Chapter 2, the temporal steering vector, $\mathbf{b}(\omega_i k)$, is given by (37).

$$\mathbf{b}(\omega_{ik}) = \begin{bmatrix} 1 & e^{j2\pi\widetilde{\omega_{ik}}} & \ldots & e^{j2\pi(M-1)\widetilde{\omega_{ik}}} \end{bmatrix}^{T}. \tag{37}$$

The coherent integration of the target returns' slices which is taken into account for point target returns and considered as a single scatterer for each target range gate [5, 6, 16, 17]. The original spatial steering vectors shown in Chapter 2 are expanded to (38) for incorporation of 3D STAP.

$$\mathbf{v}_{ch}(\theta_i, \phi_k, \mathbf{b}(\omega_{ik})) = \mathbf{e}_{ch}(\vartheta_{z,ch}(\theta_i)) \otimes \mathbf{b}(\omega_{ik}) \otimes \mathbf{a}_{ch}(\vartheta_{x,ch}(\theta_i, \phi_k)). \tag{38}$$

$\alpha_{C,ik}$ in (40) is the complex target amplitude term incorporating subarray effects, which depends on the subarray pattern for each of the target slices for each range, shown in (39).

Similarly, the clutter space time snapshot accounting for the effects of 3D STAP is

given by (45).

$$\begin{aligned}\xi_{CNR,ik} &= \frac{P_t G(\theta_i,\phi_k) g_{sub}(\theta_i,\phi_k)\lambda_0^2 {\sigma_{t,ik}}^2}{(4\pi)^3 L_S {R_i}^4 \mathbf{N}_{out,ch}} \\ &= \frac{P_t\left[|\mathbf{AF}_{ch}(\theta_i,\phi_k)|^2\left\{|\mathbf{AF}_{sub}(\theta_i,\phi_k)|^2 g_{elm}(\theta_i,\phi_k)\right\}^2\right]\lambda_0^2 {\sigma_{t,ik}}^2}{(4\pi)^3 L_S {R_i}^4 \mathbf{N}_{out,ch}}.\end{aligned} \tag{39}$$

$$\alpha_{C,ik} \tilde{} N\left(0,\ \frac{\mathbf{N}_{out,ch}\xi_{CNR,ik}}{2}\right) + iN\left(0,\ \frac{\mathbf{N}_{out,ch}\xi_{CNR,ik}}{2}\right). \tag{40}$$

$$\sigma_{t,ik} = \sigma_o(\theta_i,\phi_k) R_i \Delta\phi \Delta R \sec\psi_i,\ i = 0, 1, \ldots, N_r - 1\ and\ k = 0, 1, \ldots, N_c - 1. \tag{41}$$

$$\Delta R = \frac{C}{2B}. \tag{42}$$

$$\Delta\phi = \frac{2\pi}{N_c}. \tag{43}$$

$$\sigma_o(\theta_i,\phi_k) = \gamma \sin\psi_{ik}. \tag{44}$$

$$\chi_{C,ch,ik} = \sum_{i=0}^{N_r-1}\sum_{k=0}^{N_c-1} \alpha_{C,ik}\mathbf{e}_{ch}(\vartheta_{z,ch}(\theta_i,\phi_k)) \otimes \mathbf{b}(\omega_{ik}) \otimes \mathbf{a}_{ch}(\vartheta_{x,ch}(\theta_i,\phi_k)). \tag{45}$$

The crosscovariance of $\chi_{C,ch,ik}$ over the number of clutter patches, N_c, and range rings, N_r, returns the clutter snapshots, which are shown in (45), and the true covariance is computed using the expected value, shown in (46).

$$\begin{aligned}\mathrm{R}_{C,ch} = E\{\chi_c \chi_c^H\} = &\mathbf{N}_{out,ch}\sum_{i=0}^{N_r-1}\sum_{k=0}^{N_c-1}\xi_{CNR,ik}[\mathbf{e}_{ch}(\vartheta_{z,ch}(\theta_i,\phi_k))\{\mathbf{e}_{ch}(\vartheta_{z,ch}(\theta_i,\phi_k))\}^H \\ &\otimes \mathbf{b}(\omega_{ik})\mathbf{b}(\omega_{ik})^H \otimes \mathbf{a}_{ch}(\vartheta_{x,ch}(\theta_i,\phi_k))\{\mathbf{a}_{ch}(\vartheta_{x,ch}(\theta_i,\phi_k))\}^H].\end{aligned} \tag{46}$$

$$rank(\mathrm{R}_{C,ch}) \approx \lfloor N + (M-1)\beta \rfloor. \tag{47}$$

$$\beta = \frac{2 v_a T_{PRI}}{d_x}. \tag{48}$$

The clutter to noise ratio (CNR), $\xi_{CNR,ik}$, scales the true covariance and ,as shown in

(39), $\xi_{CNR,ik}$ heavely depends on the radar cross section (RCS) of the i^{th} and k^{th} clutter patch. Including the clutter snapshot and covariance into the spatial model described in Chapter 2 results in (49) and (50).

$$\chi_{ch} = \chi_{N,ch} + \chi_{J,ch} + \chi_{C,ch}. \tag{49}$$

$$\mathrm{R}_{ch} = \mathrm{R}_{N,ch} + \mathrm{R}_{J,ch} + \mathrm{R}_{C,ch}. \tag{50}$$

2.2.6 Subarray Modeling for the Clutter Model.

Most STAP techniques have focused on azimuth-Doppler adaptivity with less elevation effect. T. Hale's three-dimensional factored method adopts the elevation beamforming technique which introduces target height discrimination capability with enhanced clutter suppression performance [18, 19]. Since ground clutter is the main concern in this research, where the Earth's surface is stationaly, the Doppler shift to the ground clutter patch only depends on the airborn platform velocity [18].

The elevation subarray beamfroming partitions each column of the element array to a single subarray [6]. The individual computation of a snapshot from each subarray produces the maximum gain in each elevation angle and range bin, which adaptively processes for the clutter suppression, comparing it to the element-by-element snapshot computation.

2.3 STAP Processors

In J. Ward's 'Space-Time Adaptive Processing for Airborne Radar', STAP is described as the extension of adaptive antenna techniques to processors that simultaneously combine between the signals received on multiple elements of an antenna array and from multiple pulse repetition periods per CPI [4]. This section shows how KASPS is modeled to demonstrate synergistic DOF improvement with a two-stage adaptive pro-

cess: 1. Adaptive spatial null plaing 2. clutter null placing. The following sections describe the clutter model that is developed for this research and the modified algorithm method to incorporate the STAP process.

2.3.1 STAP Filtering.

The key process for STAP filtering is synthesizing the snapshot which represents the specific element, pulse and range gate for noise and interference including jammers and clutters for its adaptive filtering. There are many filters techniques that can be used for the STAP process. There are two well-known fully adaptive filtering in the radar community. One is called the optimal processor, or also called matched filter (MF). Another one is the adaptive matched filter (AMF). The difference between the filtering technique in 2.1.5 and this filtering is now **v** is a 3D space-time steering vector that steers to not only an azimuth and elevation but also to a Doppler frequency. Also, R is the true space-time covariance matrix in (51) and similarly, the AMF accounts for the NMP x 1 spatial data dividied into k unambiguous range bins. Given the assumptuion of independent, identically distributed (i.i.d) training data over the range bins, the maximum likelihood estimate of the covariance matrix is computed as in (52) and using the estimated covariance matrix, the space time AMF is written as (53).

$$\mathbf{w}_{ch} = \mathrm{R}_{ch}{}^{-1}\mathbf{v}_{ch}(\theta,\phi,\omega). \tag{51}$$

$$\widehat{\mathrm{R}_{ch}} = \frac{1}{k}\sum_{k=0}^{k-1}\chi_k{\chi_k}^H. \tag{52}$$

$$\widehat{\mathbf{w}_{ch}} = \widehat{\mathrm{R}_{ch}}^{-1}\mathbf{v}_{ch}(\theta,\phi,\omega). \tag{53}$$

2.3.2 STAP Performance Metrics.

Using R and χ formulated in 2.2.1, the filtering weight vector, w, is computed for an arbitrary and non-fluctuating target, which incorporates the ground clutter into the SINR. The SINR for the MF and AMF are computed in order to compare the ideal and estimated performance, shown in (54) and (55).

$$\mathbf{SINR}_{out,MF} = \mathbf{N}_{out,ch}\xi_{SNR}\frac{|\mathbf{w}_{ch}^{H}\mathbf{v}_{ch}(\theta,\phi,\omega)|^2}{\mathbf{w}_{ch}^{H}\mathrm{R}_{ch}\mathbf{w}_{ch}}. \tag{54}$$

$$\mathbf{SINR}_{out,AMF} = \mathbf{SINR}_{out,MF}\Big|_{\mathbf{w}_{ch}=\widehat{\mathbf{w}_{ch}}}. \tag{55}$$

$$\mathbf{SINR}_{out,SMF} = \mathbf{SINR}_{out,MF}\Big|_{\mathbf{w}_{ch,ik}=\mathbf{v}_{ch}(\theta,\phi,\omega)}. \tag{56}$$

2.4 Antenna Pattern Beam Forming and Steering

The received power from phased array systems includes noise and interference, which can be digitally nulled with digital filtering weight sets. This technique is called adaptive digital beamforming (ADBF). With subarraying, however, less ADCs are needed to handle the nulling process and also the greater spacing between the channels causes grating lobes, which results in reduced DOFs. The next two sections will discuss the different types of beamforming techniques: ADBF, subarray beam steering (SBS)-ADBF and KASPS-ADBF.

2.4.1 Subarray beam steering-adaptive digital beamforming (SBS-ADBF).

The ADBF consists of the antenna manifold is NP elements which is not subarrayed. Therefore, every element is connected to an individual ADC and the output from the ADCs are adaptively processed in the digital beam former processor with the digitally

computed filtering weight, $\mathbf{w_{ch}}$, which is the ideal processor but not used in real world system due to its high cost. This can accommodate $NP-1$ DOFs. As discussed in earlier sections, subarraying is a very effective solution to reduce cost and grating lobes that are created reducing the DOFs and significantly reducing the interference nulling capability. The main cause is that the subarray pattern's mainbeam is steered in the target look direction, which is described with the steering vector, $\mathbf{v_{sub}}$ in the Figure 4. This effect produces grating lobes in its arrayfactor, which copies the jamming power in multiple directions. In order to solve this problem, it is required to manipulate the subarray pattern to place its null at the jammers. The next section discusses this adaptive process.

2.4.2 Knowledge-aided subarray pattern synthesis-adaptive digital beamforming (ADBF).

With subarraying, the subarray pattern and digital array factor can result in degraded interference suppression performance since the grating lobes created in the digital array can align with the subarray pattern nulls, so nulls are low enough to reduce the interference. Therefore, its 'number of channel - 1: NP - 1' DOFs is as many DOFs as it can achieve with a subarray beam steering adaptive digital beamforming in the digital Beamformer (SBS-ADBF) [1]. In order to increase DOFs with use of the internal elements in subarrays, adaptive filtering weight, $\mathbf{w}_{sub,}$ needs to be applied as shown in Figure 5, which improves the subarray pattern's nulls placing ability with SBS-ADBF. Estimating the subarray covariance matrix creates a weight set that can adaptively place the subarray pattern's nulls but this requires prior knowledge of jamming signals such as jammer's elevation, azimuth and jammer power. This technique is called the KASPS-ADBF [1].

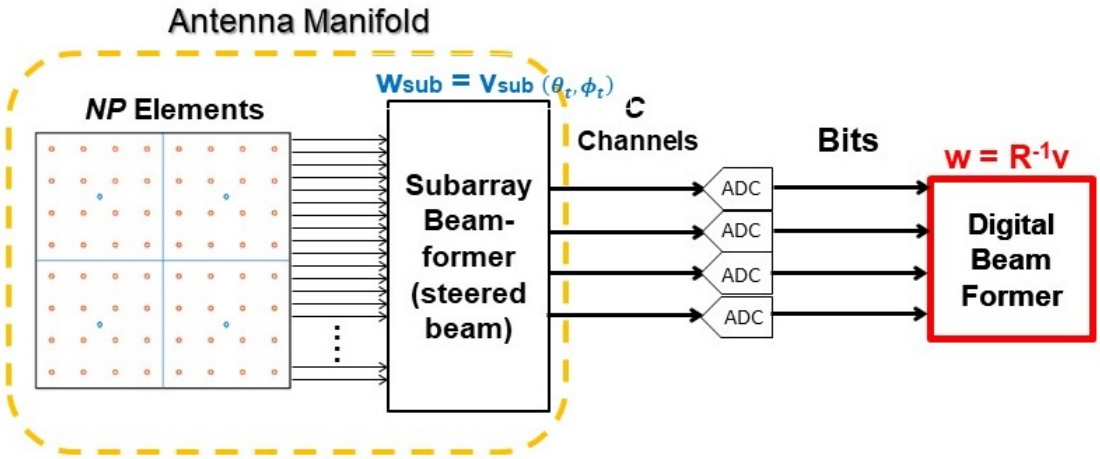

Figure 4. System processing chain of SBS-ADBF

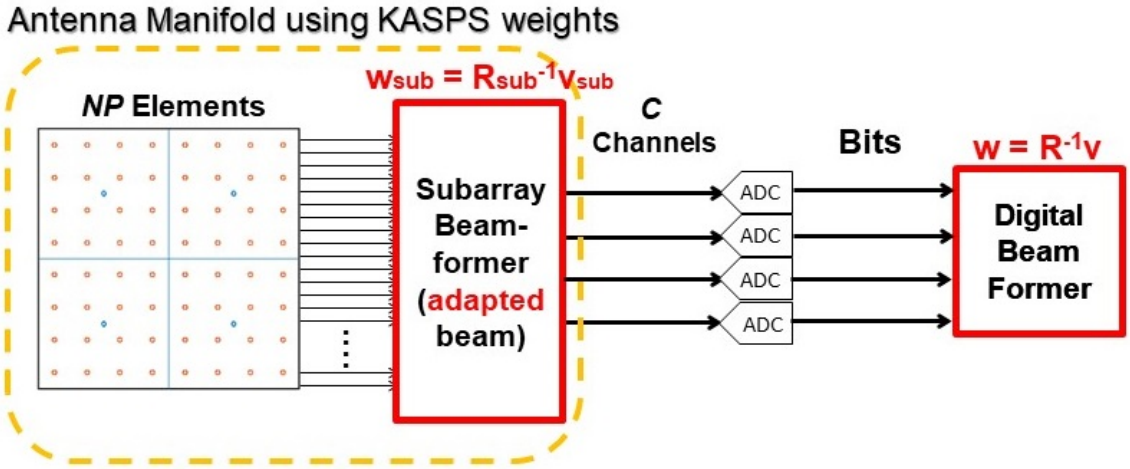

Figure 5. System processing chain of KASPS-ADBF

2.5 Model Limitations

New's KASPS-ADBF model only accounts for the spatial processing and, thus, the modeled is 2-dimension STAP which does not consider cluttered returns in KASPS-ADBF's interference model. In modern airborne radars, relative ground clutter motion affected by the phase causes angle Doppler coupling. Therefore, multi-dimensional STAP is required to accomodate Doppler returns from compound locations, which allows wideband adaptive beamforming [10].

Today's subarray systems often use overlapping of subarrays due to its sidelobe suppression and it is also more robust for canceling the array's apperture errors [1]. However, New's previous work does not use the overlapping technique.

One critical assumption made for the KASPS model is a half wavelength element spacing [1]. There will be more grating lobes produced by this spacing and it will create more ambiguity in signal and interference returns; thus, the KASPS-ADBF's performance might be more degraded. As a result, KASPS might not properly demonstrate consistent performance.

2.6 Summary

D. New's KASPS-ADBF reduces subarray's interference suppression degradation caused by misalignment of subarray pattern's nulls and digital array factor [1]. KASPS is an algorithm that produces an adaptive filtering weight in subarray beam steering by comparing every possible null direction given a jammer combination and finds a jammer combination that can most improve the SINR [1]. With the algorithm, New's research proved that KASPS achieved the higher field of regards coverage than the regular ADBF without KASPS. However, his KASPS model is not extended to 2 dimensional STAP that accounts for clutter returns and is also not modeled for overlapped subarrays or non-planar subarrays [1]. In this research, the 3-dimensional STAP will be modeled in the

KASPS algorithm and the refined algorithm will be tested with a simulation tool.

III. Methodology

This chapter discusses the overview of knowledge-aided subarray pattern synthesis (KASPS) and a method to compute the KASPS weight when clutter included. The mathematical formulation is derived and demonstrated the criteria to choose the best KASPS weight. Finally the chapter introduces the test scenarios conducted to examine the methodology.

3.1 KASPS Overview

KASPS is a spatial-only nulling technique using subarray pattern synthesis where nulls are steered based on estimated interference information. The technique allows knowledge-aided analog beamforming/null steering with subarray elements. The subarray nulls cannot be steered by the digital beamformer; the patterns are synthesized using hardware weight sets. The three pieces of information required for using KASPS are: 1. jammer location 2. jammer power 3. the antenna manifold. This thesis assumes the first and second pieces of information can be collected from off-board intel or on-board sensor packages. This is just an assumption and this thesis does not discuss of the resources or methods for acquiring this data. The previous thesis by D. New explored a method to estimate jammer location and power. The detailed mathematical formulation is shown in the next section. The third piece of knowledge needed is calibrated antenna manifold data. As stated earlier, the subarray beam pattern is created in analog hardware where temperature mutual coupling, and manufacturing tolerances require detailed array calibration in order to achieve accurate pointing angles and side lobe control. This calibration data is also the key to accurately placing subarray pattern nulls to mitigate jammers. This research assumes this calibration data exists and is of sufficient quantity and quality to support the KASPS technique.

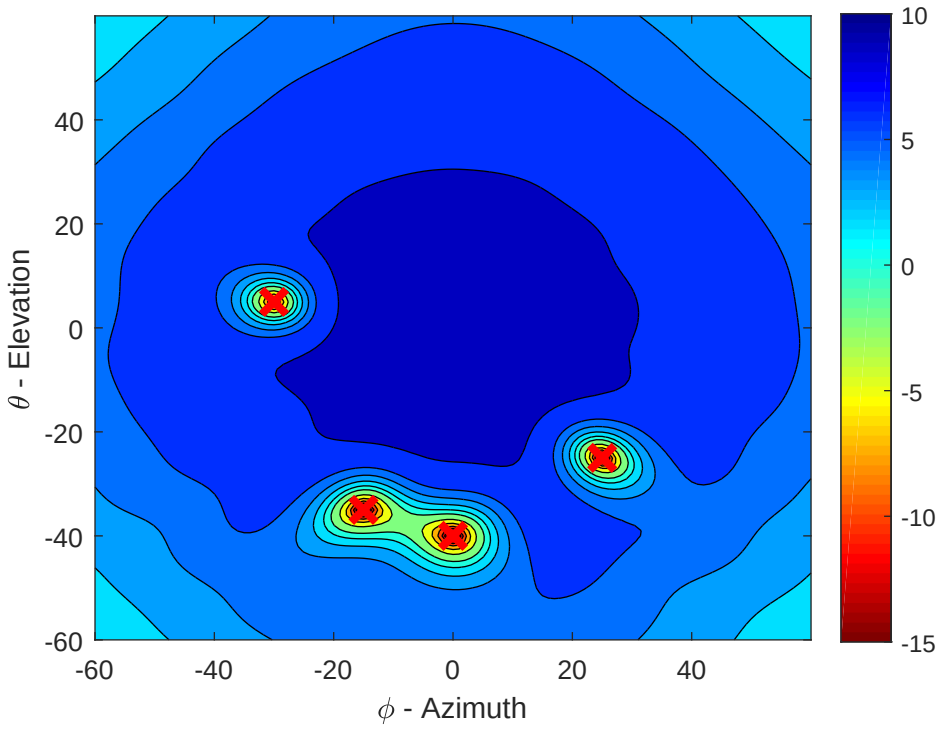

Figure 6. 8 x 8 array (non-subarray) with 64 channels and 63 DOFs

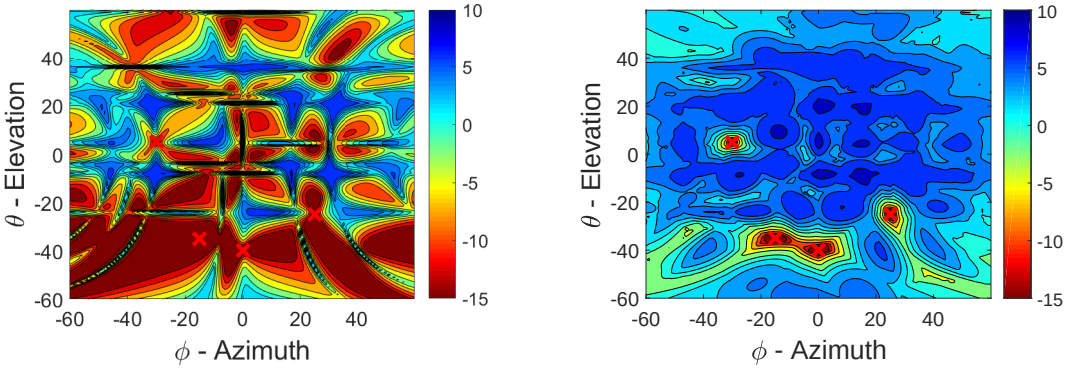

(a) 2 x 2, 4 x 4 (SBS-ADBF)

(b) 2 x 2, 4 x 4 (KASPS-ADBF)

Figure 7. Comparison between SBS-ADBF vs KASPS-ADBF

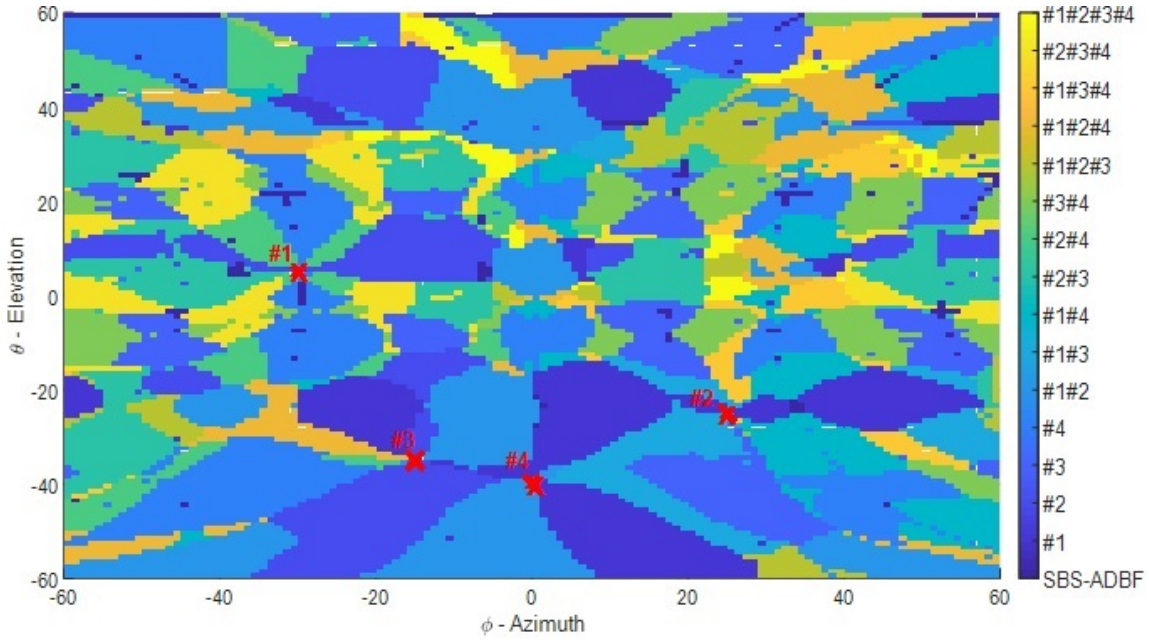

Figure 8. Nulled jammers at each target look angle

The main purpose of KASPS technique is to utilize the 'dormant' spatial nulling capacity (or spatial DOF) of the subarrays in the phased array antenna. This can mitigate some spatial interference and thus allow the limited digital DOF to be used more effectively in mitigation of space-time interference and residual spatial interference.

Figure 7 (a) and (b) illustrate the main advantage of KASPS. Figure 7 (a) depicts an 8x8, 64 element fully digital array adaptively nulling 4 jammers. The 63 digital DOFs easily nulled 4 jammers without substantial impacts throughout the field of view. However, if the 8x8 array is subarrayed into 4 channels, each containing 2x2 subarrays, the digital spatial DOF is now 4-1=3, which is one DOF short of being able to null 4 jammers. DOF non-subarray easily nulled 4 jammers without reducing signal power at the other look angle. Also, the greater channel spacing due to subarraying in causes the spatial frequency ambiguities and creates grating lobes in the digital processing. The grating lobes alias the jammer energy that comes in though the sidelobes of the subarray beampattern at additional main beam look directions. By using KASPS-ADBF,as shown in (b), the aliased jamming signals are mitigated, with a modest increase in SINR

loss except for where the jammers are located. As a result, the KASPS DOF helped mitigate the interference and improve the output SINR performance.

3.1.1 Mathematical Extension for STAP Integration.

To compute the KASPS weight, the subarray jammer covariance matrix of the jammers to be nulled synthesized. This research focuses on bounding the possible KASPS performance, while making sure KASPS does no worse than the non-KASPS solution. This requires simulating all possible KASPS null combinations based on the number of jammers present. As shown in the equation (57), spatially adaptive subarray weights are synthesized for each possible combination of jammers, to find which KASPS constraints (nulls) yield the best results.

$$\mathrm{R}_{J,sub} = \left\{\mathrm{R}_{J,sub,1}, \mathrm{R}_{J,sub,2}, \ldots, \mathrm{R}_{J,sub,m}\right\},\ (m = \#\,of\ jammers). \tag{57}$$

Using the computed 'm' number of subarray covariance matrices, create all possible jammer combination which is annotated as (58).

$$\widetilde{\mathrm{R}_{J,sub}} = \left\{\mathrm{R}_{Jcom,sub,1}, \mathrm{R}_{Jcom,sub,1}, \ldots \mathrm{R}_{Jcom,sub,2^m-1}\right\}.\ (m = \#\,of\ jammers). \tag{58}$$

The total numbers of cases is $2^m - 1$, which is the sum of combination, 'm choose n'.

$$Number\ of\ elements\ in\ \widetilde{\mathrm{R}_{J,sub}} = \sum_{n=1}^{m} \begin{pmatrix} m \\ n \end{pmatrix} = 2^m - 1.\ (m = \#\,of\ jammers). \tag{59}$$

The noise covariance matrix sized $N_{sub}P_{sub}$ x 1 is added to all the elements. The process shown so far is the subarray synthesizing process, which is the main part of the KASPS

weight computation process.

$$\widetilde{\mathrm{R}_{sub,x}} = \widetilde{\mathrm{R}_{J,sub,x}} + \mathrm{R}_{N,sub},\ (x = 1,\ 2,\ \ldots,\ 2^m - 1). \tag{60}$$

Next, the Wiener-Hopf equation is used to compute the filtering weight as seen in (61) using the noise and synthesized jammer combined covariance shown in (60). The resulting adaptive filtering weight computed is the KASPS weight for adaptive beamforming. This weight needs to be normalized with the scaling factor ρ which is the maximum amplitude among the weight vector. This normalization assumes a maximum transmit and/or receive gain at each element. This is an important practical constraint for comparing KASPS and non-KASPS performance.

$$\widetilde{\mathbf{w}_{sub,x}} = \rho \widetilde{\mathrm{R}_{sub,x}}^{-1} \mathbf{v}_{sub}(\theta_t, \phi_t),\ (x = 1,\ 2,\ \ldots,\ 2^m - 1). \tag{61}$$

Two major variables that are impacted by the subarray KASPS weights are the peak (coherent) subarray pattern gain and the subarray output channel noise. Equation (62) shows the subarray's array factor formed by the KASPS weights which gives the subarray pattern adaptive nulling capability. The KASPS weight places nulls corresponding to the jammer locations which are contained within the synthesized subarray covariance built to null the specific jammer locations.

$$\widetilde{g_{sub,x}}(\theta, \phi) = |\mathbf{AF}_{sub}(\theta, \phi)|^2 g_{elm}(\theta, \phi) = |\widetilde{\mathbf{w}_{sub,x}}^H \mathbf{v}_{sub}(\theta_t, \phi_t)|^2 g_{elm}(\theta, \phi). \tag{62}$$

The channel noise output power is also affected by KASPS weight vectors. By noncoherent gain integration, seen in (63), the noise input power is scaled by the Hermitian product of the KASPS weight vectors to produce the channel output noise power. Without KASPS, the input power scaling factor is the product of $N_{sub} P_{sub}$ which is greater

than the Hermitian product of the KASPS's weight vectors; therefore, using KASPS results in an advantageous reduction of channel noise output power.

$$\widetilde{\mathbf{N}_{out,ch,x}} = \mathbf{N}_{in,elm} F_N \left(\widetilde{\mathbf{w}_{sub,x}}^H \widetilde{\mathbf{w}_{sub,x}} \right). \tag{63}$$

The subarray pattern gain and channel noise power with the KASPS weight vecor integrated are incorporated into CNR, JNR, and SNR, which are the critical components for clutter and Jammer channel covariance matrices, shown in (64) and (65) and these numbers are used to produce the '$2^m - 1$' clutter, jammer, and noise covariance matrices which are superimposed to account for their total effect on each ikth clutter patch as seen in (67).

$$\widetilde{\xi_{JNR,n,x}} = \xi_{JNR,n} \Big|_{g_{sub}(\theta_{J,n},\phi_{J,n})=\widetilde{g_{sub,x}}(\theta_{J,n},\phi_{J,n}),\mathbf{N}_{out,ch}=\widetilde{\mathbf{N}_{out,ch,x}}}. \tag{64}$$

$$\widetilde{\xi_{CNR,ik,x}},\ \widetilde{\xi_{SNR}} = \xi_{JNR,n},\ \xi_{CNR,ik},\ \xi_{SNR} \Big|_{g_{sub}(\theta,\phi)=\widetilde{g_{sub,x}}(\theta,\phi),\mathbf{N}_{out,ch}=\widetilde{\mathbf{N}_{out,ch,x}}}. \tag{65}$$

$$\begin{aligned} \widetilde{\mathrm{R}_{C,ch,x}} = {} & \mathrm{R}_{C,ch} \Big|_{\mathbf{N}_{out,ch}\xi_{CNR,ik}=\widetilde{\mathbf{N}_{out,ch,x}}\widetilde{\xi_{CNR,ik,x}}} + \mathrm{R}_{J,ch} \Big|_{\mathbf{N}_{out,ch}\xi_{JNR,n}=\widetilde{\mathbf{N}_{out,ch,x}}\widetilde{\xi_{JNR,n,x}}} \\ & + \mathrm{R}_{N,ch} \Big|_{\mathbf{N}_{out,ch}=\widetilde{\mathbf{N}_{out,ch,x}}}. \end{aligned} \tag{66}$$

The wight vector computed in (68) is used to create the MNPx1 digital weighting vector to filter noise, clutter and jammer for the best output SINR performance.

$$\widetilde{\mathbf{w}_{ch,x}} = \widetilde{\mathrm{R}_{ch,x}}^{-1} \mathbf{v}_{ch}(\theta, \phi, \omega). \tag{67}$$

Putting all the pieces together with the SINR equation in Chapter 3, the output SINR for the 3D STAP with the KASPS weight included is given by (68). This result includes

$2^m - 1$ output SINR numbers that correspond with each KASPS weight.

$$\begin{aligned}\widetilde{\mathbf{SINR}_{out,x}} &= \widetilde{\mathbf{N}_{out,ch}}\,\widetilde{\xi_{SNR}}\,\frac{\left|\widetilde{\mathbf{w}_{ch}}^{H}\mathbf{v}_{ch}(\theta,\phi,\omega)\right|^2}{\widetilde{\mathbf{w}_{ch}}^{H}\widetilde{\mathrm{R}_{ch}}\widetilde{\mathbf{w}_{ch}}} \\ &= \left\{\mathbf{SINR}_{out,1}, \mathbf{SINR}_{out,2}, \ldots, \mathbf{SINR}_{out,x}\right\}.\end{aligned} \tag{68}$$

Finally, in order to pick the best KASPS weight set, all the output SINR values are compared and the KASPS weight that produces the maximum output SINR among $2^m - 1$ elements is picked, as shown in (69).

$$\mathbf{w}_{sub,best} = \widetilde{\mathbf{w}_{sub,l}}\Big|_{l=\arg\max_x \widetilde{\mathbf{SINR}_{out,x}}}. \tag{69}$$

3.1.2 Selective Nulling of KASPS.

As shown in the color bar seen in Figure 8, KASPS weights are used given all possible jammer combinations given 4 jammers, $2^4 - 1 = 15$, to determine the optimal adaptive nulling. If the KASPS solution produces worse performance compared to the non-adaptive subarray (SBS-ADBF) case, it is not used. The plot shows how KASPS solution producing the best output SINR is highly dependent upon the antenna mainbeam's look angle (azimuth and elevation). The plot illustrates that having KASPS null more jammers does not always produce better results. The results show that, when the antenna mainbeam approaches a given jammer location,it is generally not advangaeous to null that particular jammer using KASPS. When KASPS is used too close to the mainbeam, the target signal power returns are also reduced, which decreases the target return paower. This demonstrates that the best selection of a KASPS constraint set for nulling jammers depends on the proximity of jammers to the antenna mainbeam's look direction.

3.2 Best KASPS weights

The method to find the best KASPS weight is approached as follows. In order to gain the best interference mitigation performance, we choose the KASPS weight resulting in the highest output SINR as described in the previous section. For each KASPS weight set, its impact on the clutter must be modeled. The subarray beampatterns are used to create the clutter covariance matrix for each 'x' th KASPS constraint set, so that the impacts of the clutter are appropriately factroed into the output SINR. Each jammer imparts its degradation across all Doppler frequencies.

The output SNIR vs doppler frequency is unique for every KASPS constraint set and the best constraint set needs to be identified. The next step in evaluating KASPS performance is to compute the coverage statistics of each KASPS constraint set, which is defined as the percentage of the total output SINR across agiven output SINR value. The best KASPS weight set corresponds to a 90 % coverage statistic at the highest output SINR value. Each KASPS weight set is assessed on its coverage statistic.

3.3 CONOPS

Figure 9 shows David New's CONOPS for selecting the best KASPS constraint set. This algorithm iterates through each jammer, applying KASPS-ADBF, and compares output SINR after applying KASPS nulling to each jammer to determine which KASPS null improves SINR the most. Once the most advantageous KASPS null is selected, the algorithm tests whether or not nulling pairwise combinations of the first jammer nulled and any other jammer improves SINR. If it does, the next iteration will null combinations of those two jammers and one more previously neglected jammer (nulling combinations of 3 jammers), again, testing to see if SINR is improved. This process keeps going until running out of jammers to be nulled or until any additional contstraints fail to improve SINR. The technique attempts to fine the maximum SINR by

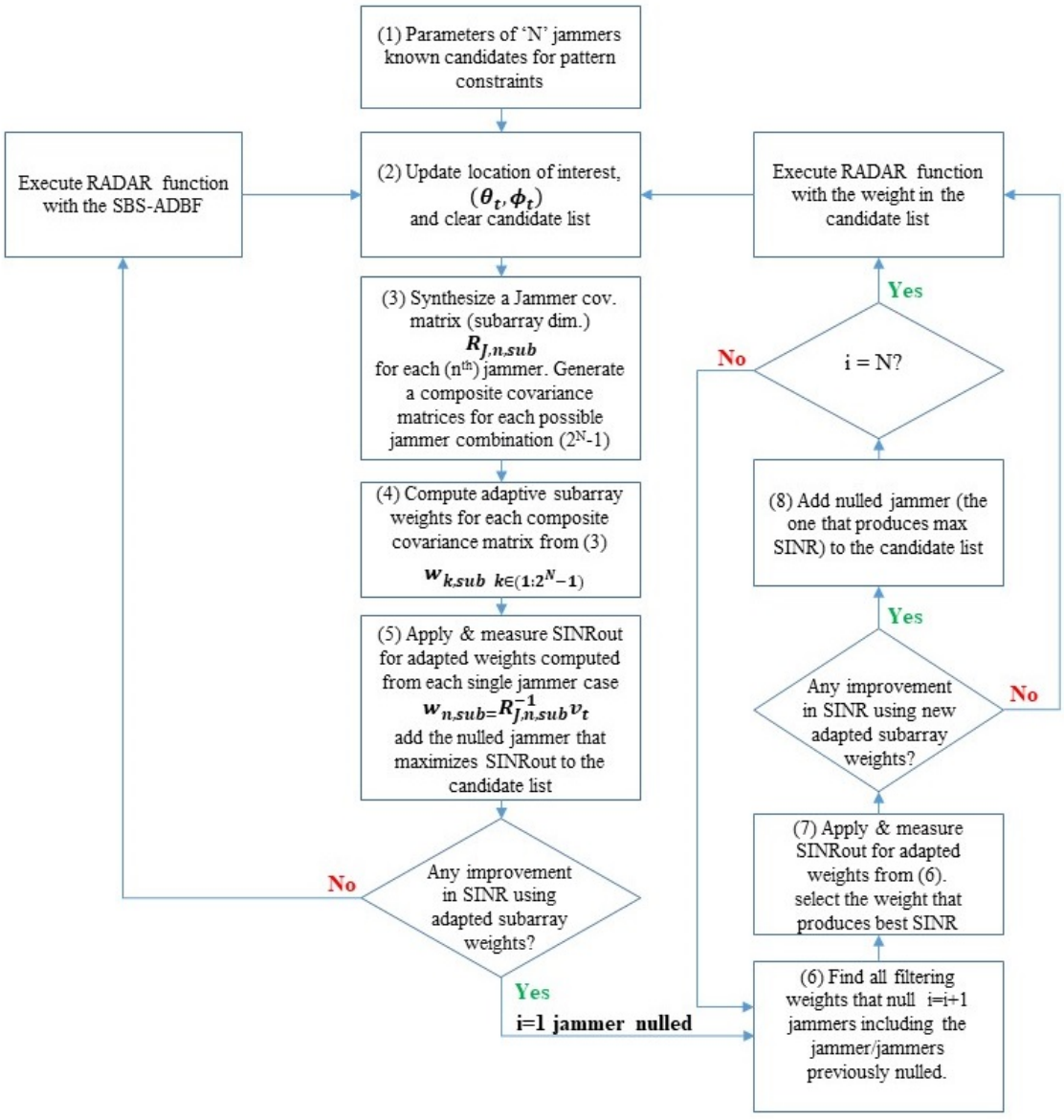

Figure 9. KASPS algorithm flow chart [1]

adding KASPS nulls while testing for SINR improvement. It was theorized that this could be done via modeling inside a beam controller, or experimentally through through iteration with the radar, which can effectively reduce the amount of radar function execution [1]. It is note worthy that in either case, this CONOPS is not an exhaustive search. This research uses an exhaustive approach, which evalutes $2^m - 1$ jammer combinations as KASPS constraints to collect all possible outcomes at each jammer or no jammer and accumulates one jammer at a time to compare all the combinations, which can effectively reduce the amount of radar function execution [1]. Moreover, this effort considers the space time case, as opposed to the spatial only case which was analyzed in previous KASPS research; this necessitates that the research account for the inclusion of clutter in this process.

3.4 Scenarios

This research explores the effects of variables on KASPS-ADBF performance. The first variable involves comparing jammer nulling results as a function of subarray and channel dimensions for both SBS-ADBF and KASPS-ADBF methods. Table 1 shows 7 unique array configurations explored including 6 subarray configurations and 1 non-subarrayed configuration. The total numbers of elements in the arrays are the same across configurations so that one can logically compare the performance between each different configuration without changing the overall power aperture. The 6 subarray configurations consist of 3 KASPS configurations and 3 non-KASPS configurations using the same array configuration for the KASPS and non-KASPS setup which allows for performance comparisons between the two methods. In order to evaluate both KASPS and non-KASPS models before characterizing performance with the Monte Carlo techniques, 5 non-random jammer locations were chosen, which are shown in Table 2, and the results were analyzed to ensure proper code functionality. The jammer power was

Table 1. 7 array configurations

Config #	ADBF type	channel size	subarray size
1	non-subarray	45 x 1	1 x 1
2	SBS-ADBF	3 x 1	15 x 1
3	KASPS-ADBF	3 x 1	15 x 1
4	SBS-ADBF	5 x 1	9 x 1
5	KASPS-ADBF	5 x 1	9 x 1
6	SBS-ADBF	9 x 1	5 x 1
7	KASPS-ADBF	9 x 1	5 x 1

Table 2. Non-random jammer parameters

Jammer#	Azimuth (degrees)	Range (km)	P_j (Watts)
1	-20	20	1.25
2	-10	25	1.25
3	20	30	1.25
4	30	25	1.25
5	40	30	1.25

Table 3. Clutter and noise parameters

N_c	H_a (m)	γ (dB)	# pulses per CPI	$N_{out,ch}$ (W)
1440	3072	-25	10	1.26e-14

fixed and a selected such that it doesn't dominate the effects of the clutter and noise.

As listed in table 3, the clutter gamma γ model parameter (-25 dB) is picked to model asphalt roads and plowed. The number of clutter patches, aircraft height, and the number of pulses per CPI are chosen to illustrate the effects of clutter and jamming on KASPS performance.

3.5 Monte Carlo Approach/Simulation

The performance of all scenarios is baselined without the presence of jammers and compared when jammers are present. The purpose of the Monte Carlo simulation is to gauge performance of the KASPS and non-KASPS systems as a function of the number of jammers and their random location within a relevant vicinity of the tar-

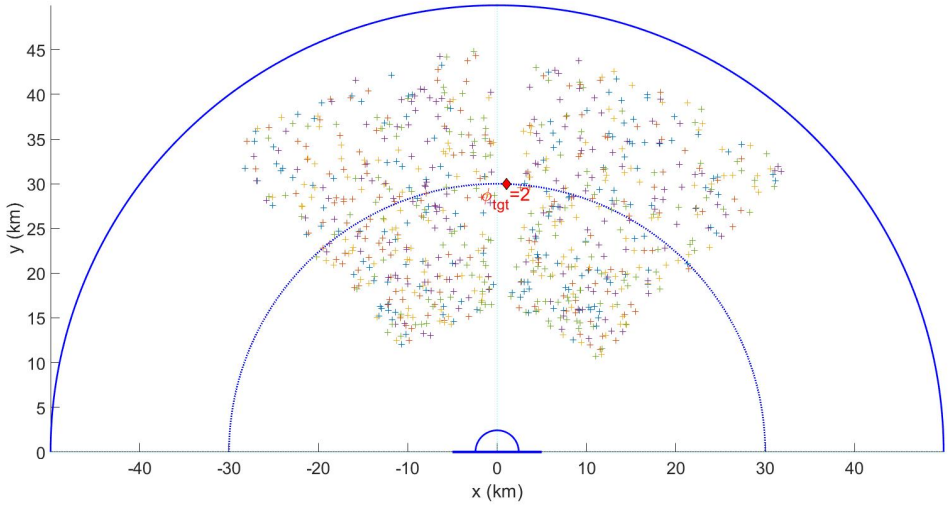

Figure 10. Randomized jammer locations in top geometry view

get. The number of jammers is a controlled parameters but their location changes randomly from run to run. This research conducts two sets Monte Carlo simulations. In the first set, each iteration of the Monte Carlo is evaluated against all the SBS-ADBF and KASPS-ADBF array configurations for randomly generated locations of 5 jammers, where the jammer positions are frozen for each Monte Carlo iteration. The jammers have the same characteristics as those derrived in table 2 but with different, random locations for each Monte Carlo interation and the jammer azimuths were randomly placed within (+ / -) 45 degrees on either side of the antenna mainbeam (pointing at the target at 2 degrees azimuth). Each Monte Carlo iteration uses 5 new jammer locations which are kept constant for all the SBS-ADBF and KASPS-ADBF array configurations. For the second set of Monte Carlo simulations, the worst performing KASPS-ADBF subarray configuration (Config #3) was used while varying the number of jammers. The jammer locations are still randomized over the Monte Carlo iterations, while increasing the number of jammers sequentially across scenarios. In each scenario, a randomly located jammer is added while the location of the prevously added jammer

remains locked in place for each iteration. The Monte Carlo results were used to generate the performance results provided in the next Chapter.

3.6 Summary

This chapter reviewed KASPS-ADBF background and showed how to incorporate KASPS into GMTI. In order to expand the KASPS model to the space-time domain, a 2D clutter model is extended and included. The KASPS weights are computed by using the synthesized subarray jammer covariance matrices with an exhaustive search across $2^m - 1$ possible jammer combinations. The best combination is found by comparing the output SINRs produced by every KASPS weight wet and choosing the one with the best output SINR at 90 % performing one. The next chapter shows the results of the static and Monte Carlo simulations.

IV. Results

This chapter presents and discusses the simulation results described in chapter 3. The experiments are divided into three parts: 1. space-time adaptive processing (STAP) simulation without jammers, 2. STAP and knowledge-aided subarray pattern synthesis (KASPS) simulation with jammers and two Monte Carlo experiments with KASPS and STAP processing. As described in chapter 3, the scenario with only clutter and noise (no jammers present) is simulated with the clutter model and ideal STAP processing. Next, jammers are added into the simulation and are compared to STAP without KASPS results in terms of signal-to-interference and noise ratio (SINR) performance, eigenvalue analysis and minimum variance (MV) analysis using the channel covariance matrices. This analysis is then extended to the results of the Monte Carlo simulations. Throughtout this chapter, the results are analyzed to determine the performance of KASPS-ADBF compared to SBS-ADBF and an idealized non-subarryed array.

4.1 STAP Simulation without Jammers

In this section, a non-subarrayed linear antenna (N:45) and subarrayed antenna (N:3, N_{sub}:15) are simulated with the parameters shown in Table 1, Table 2, and Table 3. First, the clutter to noise ratio (CNR) and the projected antenna pattern (top-down view) are plotted as shown in Figure 11. The CNR plots shown in Figure 11 depicts the clutter power computed at the channel level divided by the noise power at the element (input noise power). The channel level clutter power and element level noise is chosen to illustrate the non-coherent gain increase by N_{sub}. Figure 11 (a) shows that the CNR's amplitude is heavily influenced by each of the clutter range ring (unambiguous and ambiguous) and the antenna pattern. Since (a) is not subarrayed, the CNR's

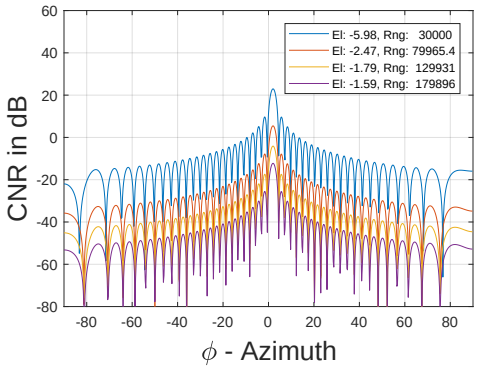

(a) CNR of non-subarray (N: 45)

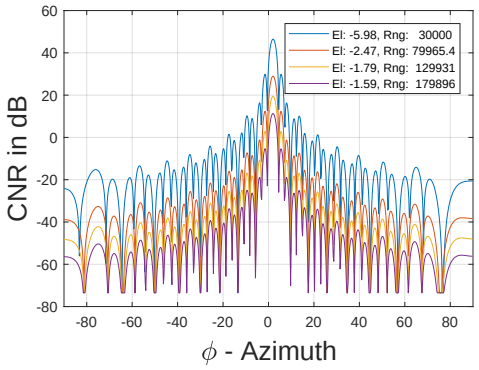

(b) CNR of subarray (N: 3, N_{sub}: 15)

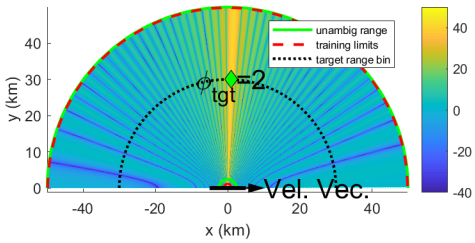

(c) Geometry top view (N: 45)

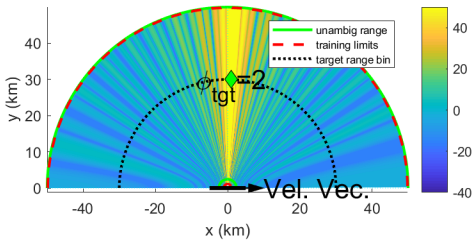

(d) Geometry top view (N: 3, N_{sub}: 15)

Figure 11. CNR and geometry top view of subarray and non-subarray from the no jamming scenario

sidelobes smoothly increase toward the mainbeam peak, while the subarrayed CNR shown in (b) exhibits an envelope embedding the ($N_s ub$:15) antenna pattern. The peak of mainbeam of (b) is 23.5 dB higher because the subarray gain (15^2) is added to each channel. Plots (c) and (d) in figure 11 are the two-way antenna patterns projected to the ground. The nulls seen in CNR plots (a) and (b) align with the nulls seen in the ground projected antenna plots shown in (c) and (d). Plot (d) also illustrates the increased receive channel gain resulting from the subarray, as well as the subarray pattern effects.

In understanding the effects of subarraying on the clutter, it is instructive to exam-

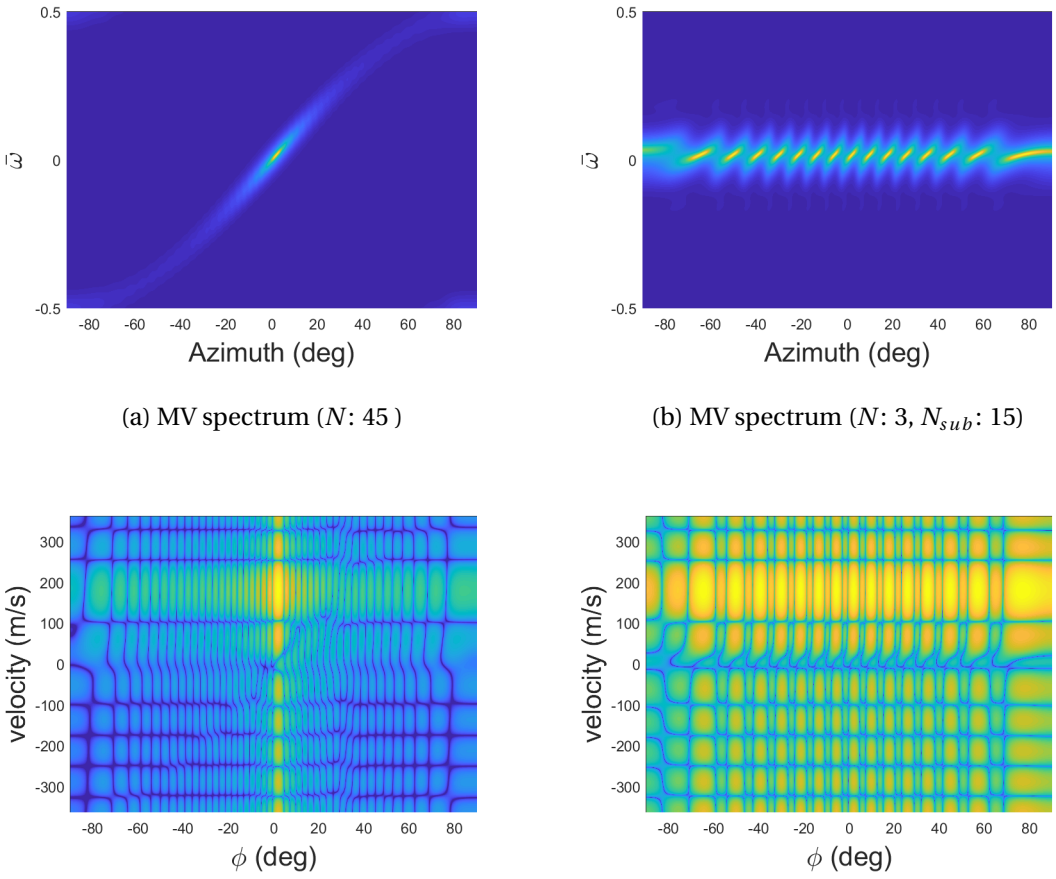

(a) MV spectrum (N: 45)

(b) MV spectrum (N: 3, N_{sub}: 15)

(c) w_{ch} (N: 45)

(d) w_{ch} (N: 3, N_{sub}: 15)

Figure 12. MV spectrum (azimuth vs Doppler frequency) and adaptive filtering response for MF (w_{ch}) of non-subarray and subarray (azimuth vs velocity)

ine the 2D interference spectrum. The minimum variance iterference spectrum plot shows the classical $\beta = 1$ spectrum without the sidelobes of a Fourier spectrum, which makes it easier to analyze the interferences as compared to a Fourier PSD plot. In figure 12 (a), a typical clutter ridge diagonal s-curve spanning across the entire azimuth range and at one elevation (-5.98 degrees) is observed in the MV plot and (c) shows the optimum digital filtering response for a target at -350 to 350 m/s that nulls the clutter. Figure 12 (b), the subarray case, shows the ambiguous interference spectrum across azimuth, where the spectrum repeats due to the increased channel spacing, d_x , due

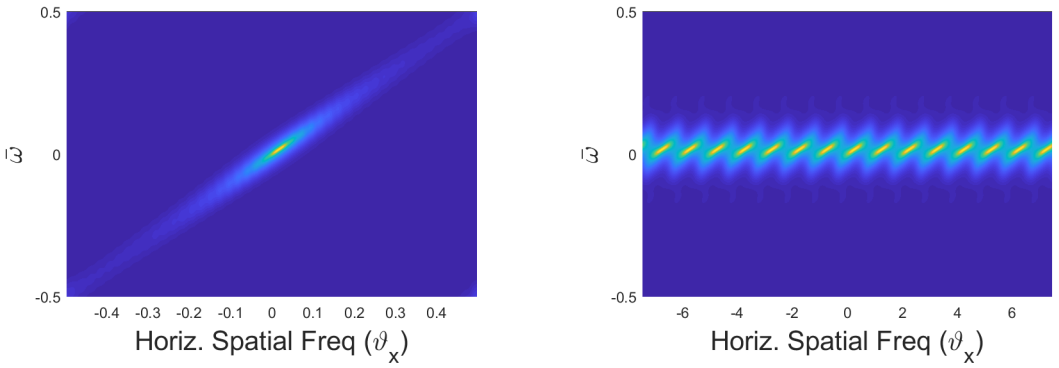

(a) MV spectrum (N: 45)

(b) MV spectrum (N: 3, N_{sub}: 15)

Figure 13. MV spectrum of subarray and non-subarray in horizontal spatial frequency (non-normalized) vs Doppler frequency

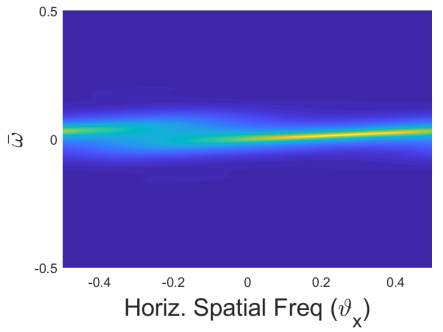

(a) MV spectrum (N: 3, N_{sub}: 15)

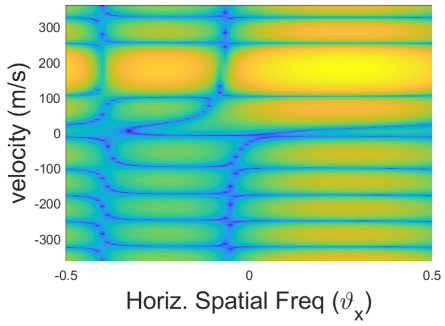

(b) w_{ch} (N: 3, N_{sub}: 15)

Figure 14. MV spectrum of subarray (N: 3, N_{sub}: 15) in horizontal spatial frequency (normalized) vs Doppler frequency

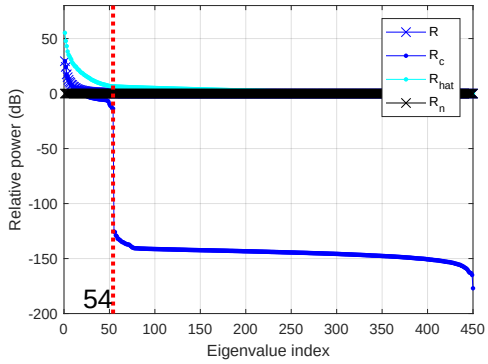

(a) eigenspectrum of subarray (45 x 1)

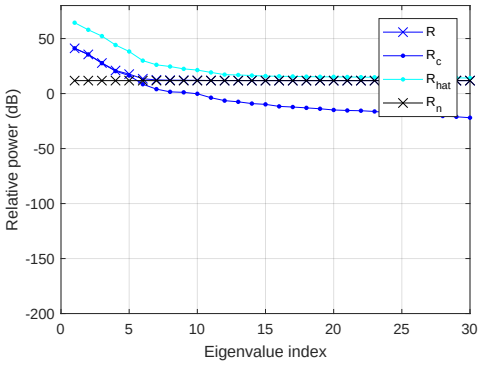

(b) eigenspectrum of subarray (3 x 1, 15 x 1)

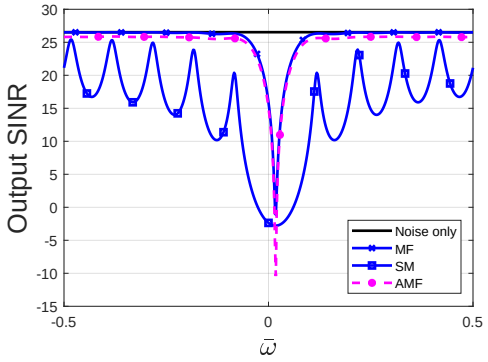

(a) ourput SINR of non-subarray(45 x 1)

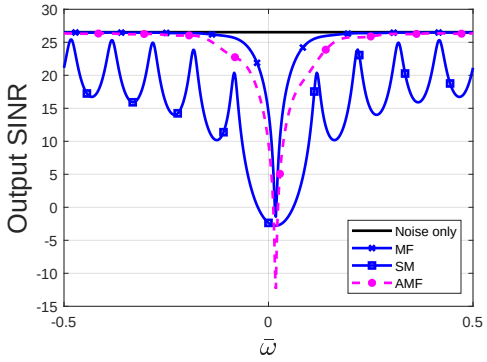

(b) ourput SINR of subarray(3 x 1, 15 x 1)

Figure 16. Eigenspectrum and output SINR comparison between non-subarray vs subarray

to non-overlapped subarraying.

In Figure 12 (b), the spatial frequency maps to -7.5 to 7.5. Figure 13 (a) and (b) shows how the spatial frequency differs between the non-subarray and subarray cases explaining why the repeated pattern is observed. Sampling the clutter ridge in figure 13 (a) results in the aliased and repeated pattern seen in Figure 13 (b). Figure 14 (a) shows the unambiguous clutter spectrum depicted within the unambiguous range of the spatial frequency from figure 13 (b). In this simplistic side-looking $\beta = 1$ clutter scenario, the clutter rank is well within the available DOF in both the subarrayed and non-subarrayed case; this is shown in the eigen spectrum in figure 15. One will also

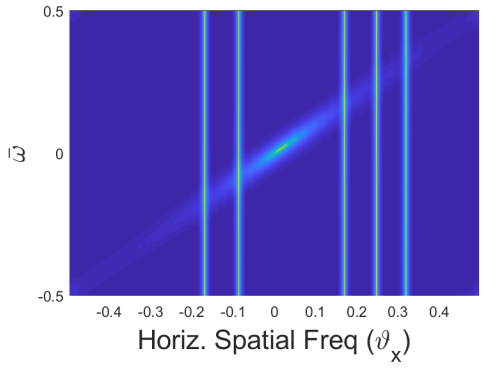

(a) MV (45 x 1)

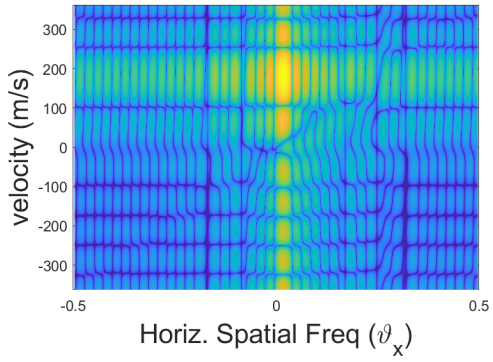

(b) channel matched filtering weight (45 x 1)

Figure 17. MV spectrum and matched filter response of non-subarray in spatial frequenccy

notice when comparing the eigen spectrums of the subarrayed and non-subarrayed systems that the noise covariance matrix's power is increased by subarraying. This is due to non-coherent noise gain through the subarray (15 x 1). Another observation is the large drop in DOFs seen in the non-subarray eigenspectrum. Plot (a) in figure 16 has a 449 DOFs from 10 pulses and 45 elements/channels while the subarray has 29 DOFs from 10 pulses and 3 channels. The plots (a) and (b) in figure 16 show that in both case, the rank of the interference (relative to the noise floor) is less tan the available DOFs, and figures 16 (c) and (d) shows very similar performance for both cases. This shows that subarraying in this case is enormously efficient, resulting in very similar

performance to the non-subarrayed case but with 15 times less channels.

4.2 STAP Simulation with Jammers

The second part of thesis investigation introduces five jammers into the radar simulation. Both SBS-ADBF and KASPS-ADBF are evaluated in each subarray configuration. As shown in Figure 17a, the five jamming signals appear as five vertical lines showing that the jammers are not dependent upon the Doppler frequency. In Figure 17b, each jammer resides at a unique spatial frequency and the adaptive filtering response in Figure 17b can be seen putting spatial nulls on both the clutter ridge and the jammers.

As discussed in chapter 3, all possible KASPS constraint sets are computed and evaluated with coverage statistics for each. A coverage percentage of 90 % was arbitrarily chosen for comparing performance of the Doppler frequencies are above that ouput SINR value. The plot in Figure 18 shows an example of this where all possible jammer combinations (i.e. KASPS constraints) are shown according to the percentage of the field of regard versus output SINR corresponding to each jammer combination. The best KASPS result is determined to be the jammer combination that gives the highest output SINR at the 90 percent point. From Figure 18, it is evident that in this particular case, the combination of nulling jammer 2 and jammer 4 with the subarray gives the best overall performance.

Figure 19b shows the interference spectrum after applying KASPS, for which nulls are synthesized and placed on jammer 2 and jammer 4 by the subarray pattern. Figure 19a shows that the SBS-ADBF does not null the jammers that aliased into the spectrum at a approximate spatial frequency of 0.2, while the KASPS subarray pater does in Figure 19b.

The second and fourth vertical lines in the MV plot shown in Figure 17a corre-

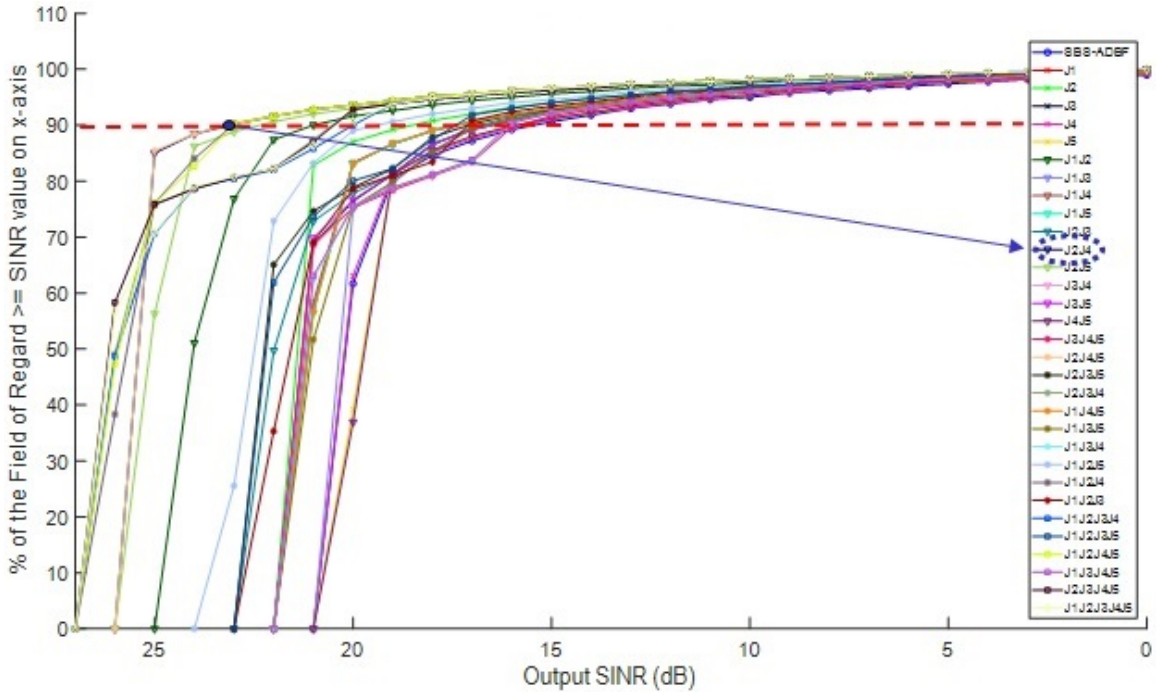

Figure 18. Percent of the field of regard greater than or equal to each given output SINR value vs the output SINR values for all possible jammer combinations

sponds to the two jammers that KAsPS tries to null.

Figure 19a shows the MV spectrum of the subarrayed using SBS-ADBF's unambiguous spatial frequency range (-0.5 to 0.5). Aliasing occurs due to subarraying and creates spatial frequency ambiguities due to the increased channel spacing. Note that unlike the clutter analysis depicted in Figures 12-16, this antenna is subarrayed into (5 x 1 , 9 x 1) subarrayed channels. Also note that with five channels and five jammers, the MV spectral estimator lacks the required DOFs to accurately depict the locations of the 5 jammers in the minimum variance spectrum estimate in Figure 19a.

However, with KASPS nulling jammers 2 and 4, the 3 remaining jammers can be accurately depicted by the 5 spatial DOFs in the spectrum estimate of Figure 19b. Taking aliasing into account, the remaining jammers (1,3 and 5) should have spatial frequencies of +0.45, -0.45 and -0.2, respectively.

As shown in Figure 19b, the residual jamming energy at 0.2 in Figure 19a does not

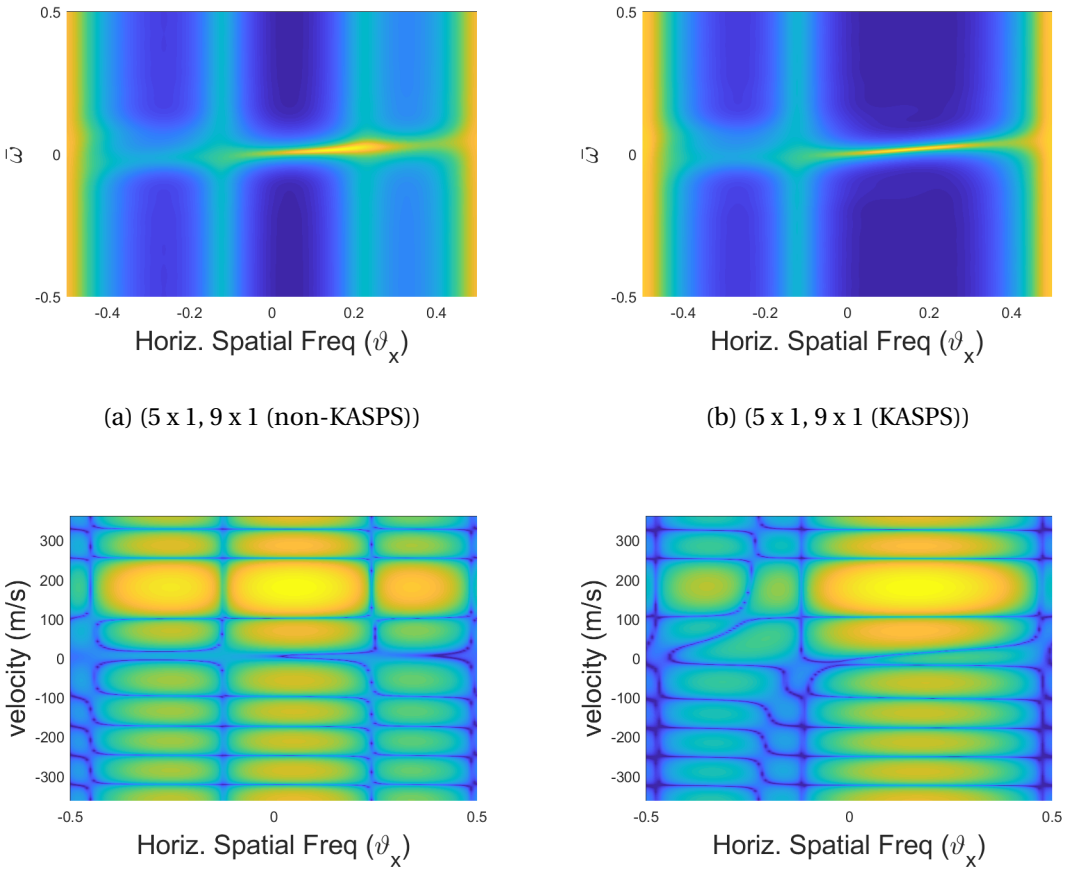

(a) (5 x 1, 9 x 1 (non-KASPS))

(b) (5 x 1, 9 x 1 (KASPS))

(c) (5 x 1, 9 x 1 (non-KASPS))

(d) (5 x 1, 9 x 1 (KASPS))

Figure 19. MV spectrum of subarray and non-subarray in normalized spatial frequency

appear. This indicates that jammers 2 and 4 were nulled with KASPS. This mitigation of jammers 2 and v via KASPS can significantly improve the overall SINR performance. Figure 20 compares the eigenvalue spectrum of the interference under ADBF, SBS-ADBF, and KASPS-ADBF. First note that the magnitude of eigenvalues in (a), (b) and (c) are slightly different. As described in chapter 3, the channel noise power of KASPS-ADBF is slightly less then SBS-ADBF because the KASPS weight set is not uniform amplitude. Therefore, the highest relative noise power given the three configurations is achieved by the SBS-ADBF with the next highest being the KASPS-ADBF and the non-subarray's noise floor being the lowest, normalized to 0 dB.

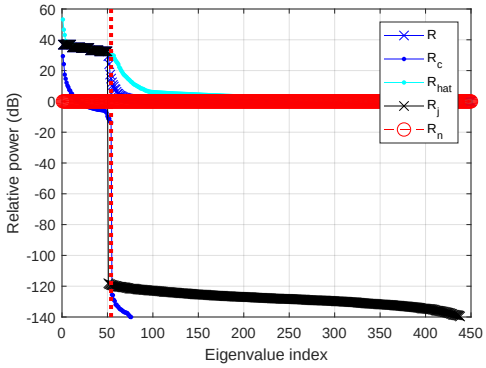

(a) (45 x 1)

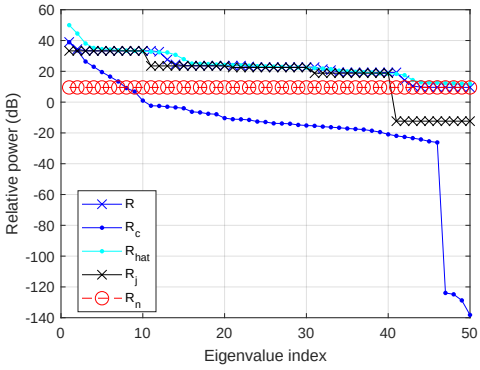

(b) (3 x 1, 15 x 1 (non-KASPS))

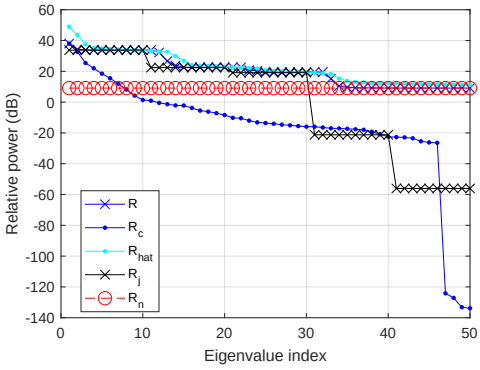

(c) (3 x 1, 15 x 1 (KASPS))

Figure 20. MV spectrum of subarray and non-subarray in degrees

Figure 20a shows that the non-subarray array has many more DOFs than the rank of the interference, providing an optional opportunity to mitigate interference. As shown in Figure 20a, in figure 20, R_J consumes 50 DOFs of the 450 total DOFs produced with 10 pulses and 45 channels, while both non-KASAPS and KASPS shown in (b) and (c) shows the 50 DOFs produced with the 5 channels, nearly consumed by the interference subspace. The R_J of SBS-ADBF in (b) shows that nulling the fours above the noise floor consumes 40 of the 50 DOFs. Even though the last jammer of the five jammers has eigenvalues lower than the noise floor, the combination of the clutter and jamming interference still results in lower output SINR performance. In figure 21b, the match

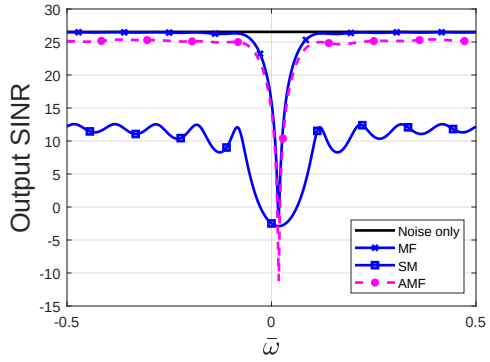

(a) non-subarray (45 x 1)

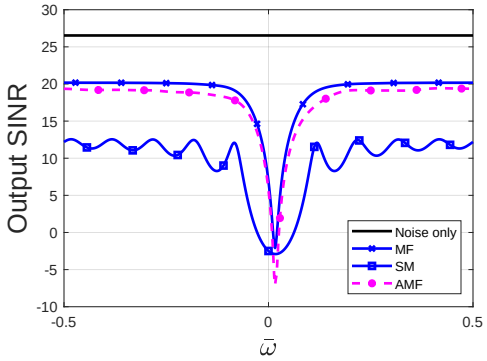

(b) subarray (3 x 1, 15 x 1 (non-KASPS))

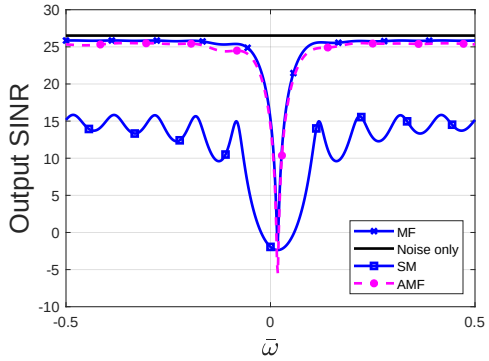

(c) subarray (3 x 1, 15 x 1 (KASPS))

Figure 21. output SINR comparison between non-subarray, non-KASPS and KASPS

filter output is reduced about 5 dB from non-subarray MF's output SINR. The eigen spectrum of KASPS-ADBF in Figure 20c shows that the last two jammers are mitigated to beneath the noise floor by KASPS nulling jammer 2 and jammer 3. Figure 21c shows that the output SINR of MF when using KASPS improves on the SBS-ADBF's MF output SINR by 5 dB, which is almost the same output SINR of the non-subarray case shown in Figure 21a which is a significant improvement over the non-KASPS subarray seen in Figure21b especially given the reduced complexity and cost enabled by the subarray

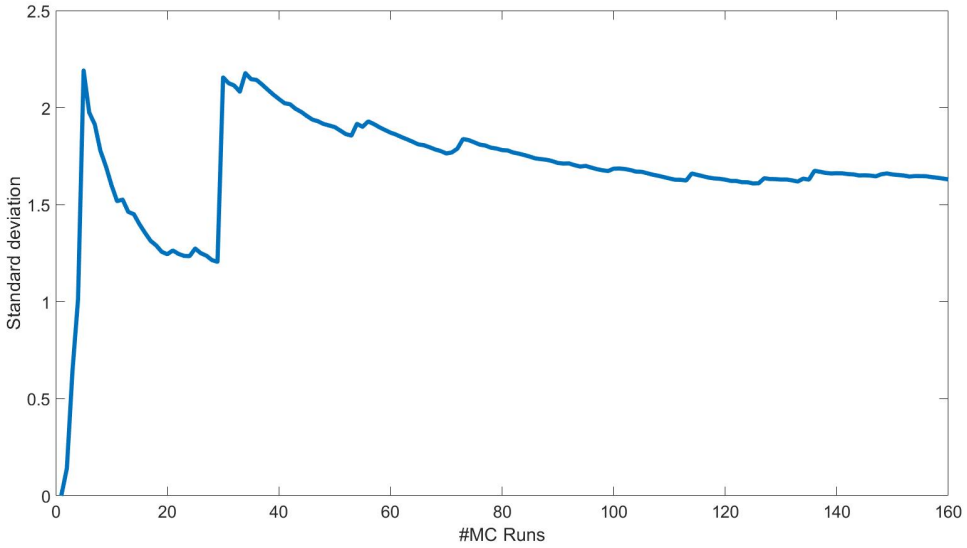

Figure 22. Determining the minimum optimal number of monte carlo trials

4.3 Monte Carlo Simulations

The results in the previous section indicate that KASPS can improve performance over standard subarraying, but more scenarios need to be explored to better understand KASPS and non-KASPS respective performances. In order to more completely characterize the relative performance of KASPS, this research conducts two Monte Carlo tests: 1. randomizing five jammer locations on 7 array configurations, 2. Evaluating configuration #3 (N: 3, N_{sub}: 15) against an increasing number of jammer (0 to 5). The minimum number of Monte Carlo runs required is determined by plotting the standard deviation of the output SINR data versus the number of Monte Carlo runs using the worst case scenario, which is configuration 3 with 5 jammers present. In the interval between 140 to 160 Monte Carlo runs, the error of the standard deviation converges to 1 %, seen in Figure 22. Therefore, 160 trials is picked for the number of Monte Carlo iterations. Figure 23a shows the result of the Monte Carlo test 1, which is testing five randomized jammer locations on 7 configurations. In the figure, the configuration that produces the highest output SINR point at 90 % of field of regard occurring

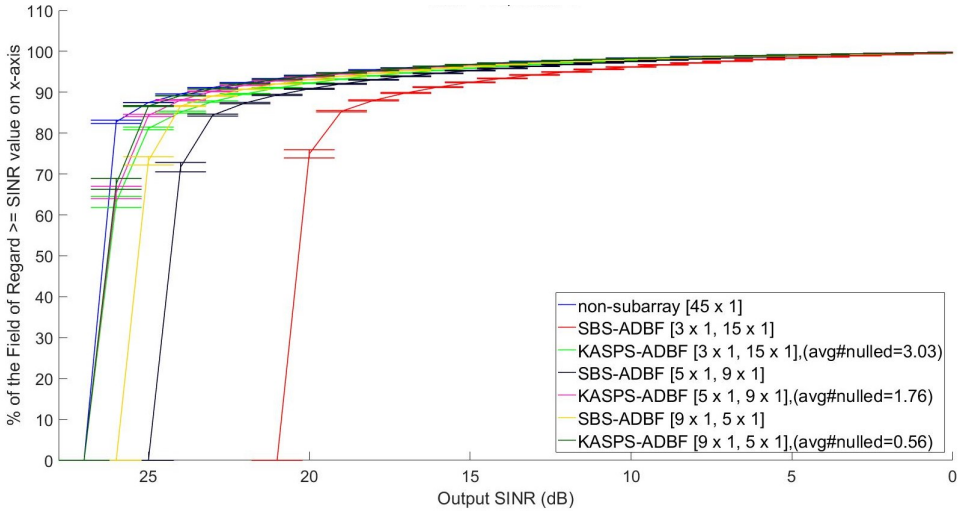

(a) 160 MC runs for KASPS and non-KASPS with diffrent size array configurations

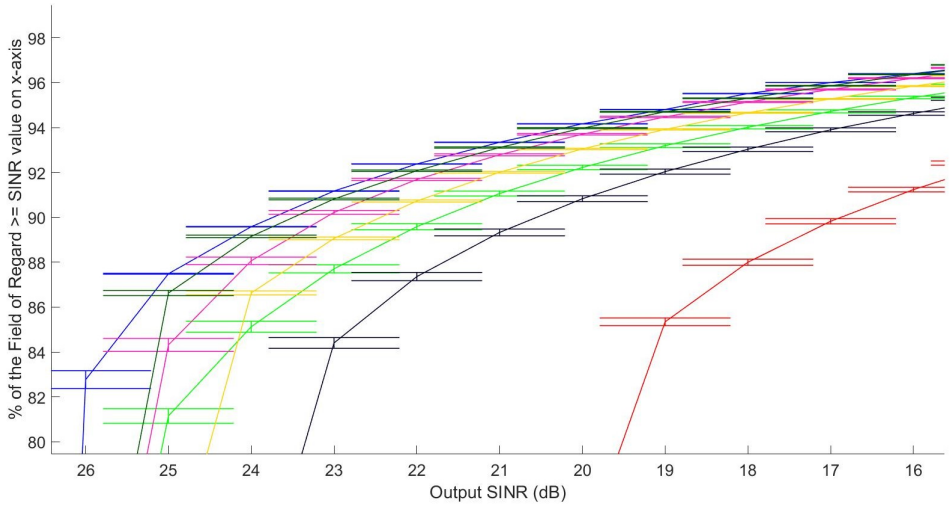

(b) zoomed in view of (a)

Figure 23. Monte Carlo test simulated for 7 array configurations

at the SINR point is the non-subarray (N: 45) as expected and the next highest one is KASPS-ADBF (N: 9, N_{sub}: 5) and the rest of the order from the highest to the lowest is as follows: KASPS-ADBF (N: 5, N_{sub}: 9), KASPS-ADBF (N: 5, N_{sub}: 9), SBS-ADBF (N: 9, N_{sub}: 5), KASPS-ADBF (N: 3, N_{sub}: 9), subarray beam steering (SBS)-ADBF (N: 5, N_{sub}: 9) and SBS-ADBF (N: 3, N_{sub}: 15). This result illustrates that all KASPS-ADBFs outperforms SBS-ADBFs except for SBS-ADBF (N: 9, N_{sub}: 5) and KASPS-ADBF (N: 3, N_{sub}: 9). The more the channels are, the higher the output SINR performance they produce so 9 channels without KASPS nulling can null 5 jammers better than 3 channels with KASPS, which may be the case. The average number of nulling conducted by KASPS varies by the dimension of the array, which is annotated in the legend of the plot in Figure 23a. The result shows that more N_{sub} results in more average number of nulling with KASPS.

KASPS-ADBF (N : 3, N_{sub} : 15), SBS-ADBF (N : 5, N_{sub} : 9) and SBS-ADBF (N : 3, N_{sub}: 15). This result illustrates that all KASPS-ADBFs outperform SBS-ADBFs except for SBS-ADBF (N : 9, N_{sub} : 5) which outperformed KASPS-ADBF (N : 3, N_{sub} : 15). The greater the number of channels are, the higher the output SINR performance they produce so 9 channels without KASPS nulling can null 5 jammers better than 3 channels with KASPS, which is the reason that SBS-ADBF (N : 9, N_{sub} : 5) which outperformed KASPS-ADBF (N: 3, N_{sub}: 15). The average number of jammers nulled by KASPS varies by the dimension of the array, which is annotated in the legend of the plot (a). The result shows that more N_{sub} results in more average jammers nulled with KASPS. The next Monte Carlo test involves iterating the number of jammers with each Monte Carlo run with the first iteration having no jammers present. With each successive Monte Carlo iteration a single, randomly located jammer is added with the location of the previously added jammer being locked in place for successive iterations. The jammer number varies from 0 to 5 jammers following this pattern and each

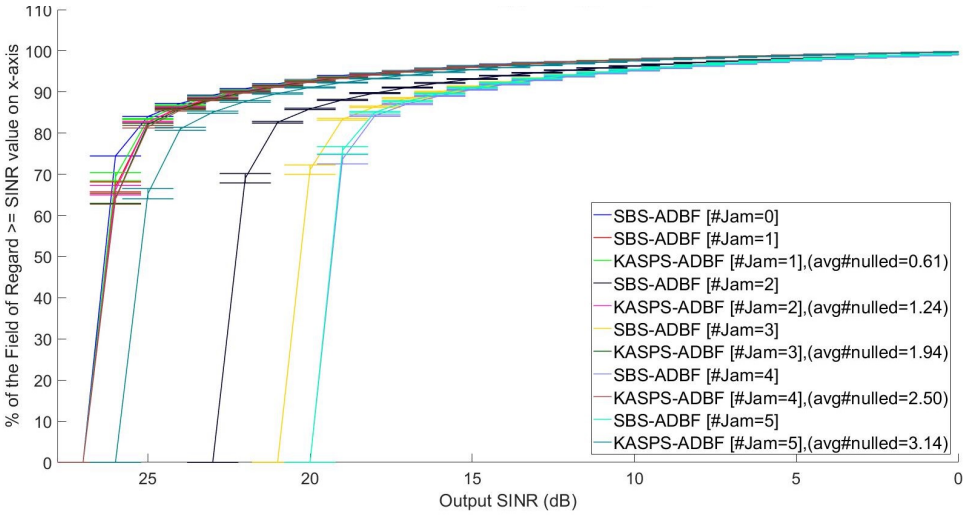

(a) 3 x 1, 15 x 1 (Monte Carlo simulation of SBS-ADBF and KASPS-ADBF) with randomly located jammers incremented from 0 to 5

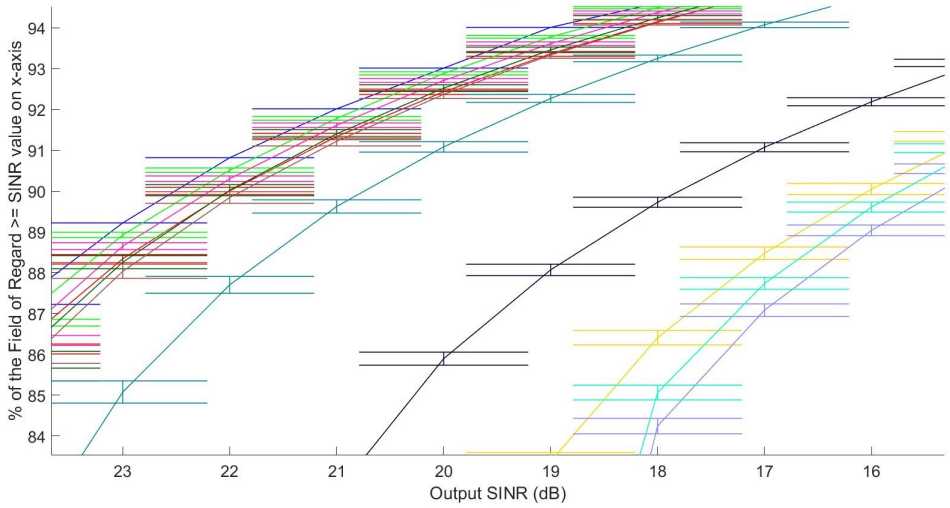

(b) zoomed in view (a)

Figure 24. Monte Carlo test with jammer number incrementally increased

Monte Carlo run uses tests the lowest performing KASPS-ADBF subarray (N: 3, N_{sub}: 15), shown in (a) of figure (b). Since including more jammers involves consuming more degrees of freedoms (DOFs), the output SINR performance decreases with as the number of jammers increases for both SBS-ADBF and KASPS-ADBF cases. One exception for this trend is SBS-ADBF with 5 jammers which narrowly exceeds the case with 4 jammers. The reason might be caused by some MATLAB's computation precision issue or that some nuance of the SBS-ADBF performs better with the 5 jammer geometry. The other trend demonstrated in plot (a) is that the KASPS-ADBF configurations outperforms the SBS-ADBF configurations except for the SBS-ADBF configuration with 1 jammer included which produces better result when compared to the KASPS-ADBF configuration when nulling 5 jammers. It is assumed that KASPS with 5 jammers will have a lower performance than SBS-ADBF with 1 jammer due to DOFs. The average number of nulled jammers increases as the number of jammers added as shown in the legend of the plot (a).

The next Monte Carlo test is increasing jammer numbers from 0 to 5 on 15 elements of 3 subarrays, shown in Figure 24a. Since including more jammers mean consuming more DOFs, the output SINR performance decreases with the more jammers for both SBS-ADBF and KASPS-ADBF cases. One exception for the trend is SBS-ADBF with 5 jammers included slightly exceeds the one with 4 jammers included. The reason might be caused by some MATLAB's computation precision issue. The other trend demonstrated in Figure 24a is KASPS-ADBF configurations outperforms the SBS-ADBF but SBS-ADBF with 1 jammer included produces better result than KASPS-ADBF nulling 5 jammers. It is assumed that Even with KASPS, having 5 jammers is very severe condition so SBS-ADBF with 1 jammer included can perform better than the KASPS-ADBF. The average number of nulled jammers increases as the number of jammers added as shown in the legend of Figure 24a.

4.4 Summary

The chapter states the results of the test scenarios described in chapter 3. 2-dimensional (2D) STAP including jammers and clutter is simulated on non-subarray, SBS-ADBF, and KASPS-ADBF. The result demonstrated that the KASPS-ADBF selectively nulls the jammers and improves the output SINR. The SBS-ADBF suffers from jammer power aliasing which is caused by spatial frequency ambiguity due to the increased channel spacing. The results show that the KASPS selected jammers to be nulled, which saves DOFs and improves the SINR output and which proves that subarraying with KASPS-ADBF can be a great solution which produces better results even with lower complexity and cost. The Monte Carlo test results validate this assertion with a large statistical significance and shows that the KASPS-ADBF outperforms the SBS-ADBF even when including more jammers on KASPS-ADBF.

V. Conclusion

This thesis investigates how to mitigate interference using knowledge-aided subarray pattern synthesis (KASPS) and space-time adaptive processing (STAP). This research investigated a method to include the effects of clutter on David New's KASPS-adaptive digital beamforming (ADBF). This research extended David New's spatial only STAP KASPS-ADBF to the space-time KASPS. Subarraying can reduce cost and hardware complexity by reducing the number of analog-to-digital converters (ADCs) for phased array systems but it does have some limitations. Subarraying reduces the number of channels as compared to non-subarraying and also causes decreases in jammer nulling capability due to grating lobes. For non-overlapped subarraying aliasing due to the spatial frequency ambiguity also occurs.

David New's KASPS can improve subarray's nulling capability by using calibrated hardware to perform KASPS. While David New's research considers radar operations in the airborne moving-target indication (AMTI) case only, this research utilizes KASPS for higher fidelity ground moving target indication (GMTI) radar operations which are degraded by the strong ground clutter. In order to model clutter with KASPS, the Doppler frequency variable was introduced; this variable is used by the temporal steering vector which is incorporated into the space-time snapshot at each range ring and the clutter to noise ratio (CNR) which accounts for the Gamma clutter model. Subarray pattern synthesis is conducted by creating all possible jammer nulling combinations at a target range and azimuth using pre-estimated jammer locations and power. The adaptive filtering weights are computed with each synthesized jammer covariance matrix creates the KASPS weights. In this research, the KASPS weight is applied to model output channel noise and CNR. The channel output noise modeled in David New's KASPS only accounts for the subarray gain and ignores the scaling effect of the KASPS weight. The CNRs are affected by KASPS for each clutter patch are superimposed and used to form

a noise, jammer and clutter covariance matrix. All this explains how the clutter effect is incorporated into David New's previous KASPS research. In this research, an exhaustive search using the coverage statistics is used to find the best KASPS weight candidate, which is the KASPS weight that produces the best output signal-to-interference and noise ratio (SINR) performance among all candidates.

5.1 Contributions

There are three contributions made by this research. First, KASPS-ADBF is combined with the space-time adaptive processing with the addition of KASPS to be applied to clutter, which allows KASPS to be applied to ground moving target indication GMTI. A criteria to select the KASPS weight from many combinations including with clutter and STAP is developed and tested. Finally the channel noise power reduction with KASPS-ADBF is discovered.

5.2 Future Work

Several options for further study to continue this research are discussed in this section. To examine the KASPS technique with more generalized phased array models, this process needs to be extended to 3-dimensional (3D) STAP by utilizing planar arrays, overlapped and/or circular subarrays. Also spectral estimation techniques can be developed for estimating jammer locations and jammer power with the collected intel. The sensitivity analysis conducted in the previous work included creating errors for the antenna manifold, jammer locations, etc with using KASPS and an extension of this work is to test these things with clutter. It is also important to explore the sensitivity of KASPS to interference location errors. More work can also be performed to develop more efficient algorithms for finding the best KASPS weight. Finally, the proof of concepts using physical subarray systems can be conducted to test the real world

feasibility.

5.3 Final Thoughts

The necessity of the electronic protection (EP) continues to rise as our adversaries' increase their electronic attack (EA) capabilities. The use of KASPS can improve overall radar systems performance by nulling jammers with subarray KASPS weights. KASPS-ADBF mitigates grating lobe ambiguities caused by non-overlapped subarrays and it utilizes dormant degrees of freedoms (DOFs) inherent in the subarrays to null spatial-only interference, freeing up digital DOFs to mitigate space-time interference more effectively. KASPS can boost a system's spatial nulling capacity and synergistically mitigate DOFs consumption caused by both jammers and clutter.

Bibliography

1. D. A. New, "Interference suppression using knowledge-aided subarray pattern synthesis," M.S. thesis, Air Force Institute of Technology, 2015.

2. R. J. Mailloux, *Phased Array Antenna Handbook*, Artech House Publishers, second edition, 2005.

3. C. J. Baker G. W. Stimson, H. D. Griffiths, *Stimson's Introduction to Airborne Radar*, SciTech Publishing, Edison, NJ, 2014.

4. J. Ward, "Space-time adaptive processing for airborne radar," in *IEEE Colloquium on Space-Time Adaptive Processing (Ref. No. 1998/241)*, Apr 1998, pp. 2/1–2/6.

5. T. B. Hale, *Airborne radar interference suppression using adaptive three dimensional techniques*, Ph.D. thesis, Air Force Institute of Technology, 2002.

6. P. M. Corbell, *Adaptive illumination patterns for radar applications*, Ph.D. thesis, Air Force Institute of Technology, 2006.

7. W. L. Melvin and A. G. Showman, "Performance results for a knowledge-aided clutter mitigation architecture," in *Radar Systems, 2007 IET International Conference*, 2007, pp. 1–5.

8. W. L. Melvin and J. A. Scheer, *Principles of Modern Radar Vol. II: Advanced Techniques*, SciTech Publishing, Edison, NJ, 2008.

9. A. J. Fenn, *Adaptive Antennas and Phased Arrays for Radar and Communications*, Artech House Publishers,, 2008.

10. J. R. Guerci, *Space-Time Adaptive Processing for Radar*, Artech House Publishers,, Norwood, MA, 2003.

11. D. C. Youla, "Multichannel detection," Tech. Rep., Atlantic Research Corporation Technical Report, April 1959.

12. Richard Klemm, *Applications of space-time adaptive processing*, The Institution of Engineering and Technology, 2004.

13. S. Haykin, "Cognitive radar: a way of the future," *IEEE Signal Processing Magazine*, vol. 23, no. 1, pp. 30–40, Jan 2006.

14. J. R. Guerci, R. M. Guerci, M. Ranagaswamy, J. S. Bergin, and M. C. Wicks, "Cofar: Cognitive fully adaptive radar," in *2014 IEEE Radar Conference*, May 2014, pp. 0984–0989.

15. G. Sanford and L. Klein, "Increasing the beamwidth of a microstrip radiating element," *Antennas and Propagation Society International Symposium*, vol. 17, 1979.

16. T. B. Hale, "EENG678 Adaptive Interference Suppression for Radar," Class Note, Air Force Institute of Technology, 2005.

17. M. Rangaswamy, "An overview of space-time adaptive processing for radar," in *Radar Conference*, 2003, pp. 45–50.

18. T. Hale and M. Temple, "Clutter Suppression Using Elevation Interferometry Fused with Space-Time Adaptive Processing," *IEEE Electronics Letters*, , no. 37(12), pp. 793–794, 2001.

19. T. B. Hale, M. A. Temple, M. C. Wicks, J. F. Raquet, and M. E. Oxley, "Performance characterisation of hybrid space-time adaptive processing architecture incorporating elevation interferometry," *IEEE Proceedings - Radar, Sonar and Navigation*, vol. 149, no. 2, pp. 77–82, Apr 2002.

REPORT DOCUMENTATION PAGE

Form Approved
OMB No. 0704–0188

1. REPORT DATE *(DD–MM–YYYY)*	2. REPORT TYPE	3. DATES COVERED *(From — To)*
06–14–2018	Master's Thesis	Sept 2016 — Jun 2018

4. TITLE AND SUBTITLE

MITIGATING INTERFERENCE WITH KNOWLEDGE-AIDED SUBARRAY PATTERN SYNTHESIS AND SPACE TIME ADAPTIVE PROCESSING

5a. CONTRACT NUMBER

5b. GRANT NUMBER

5c. PROGRAM ELEMENT NUMBER

6. AUTHOR(S)

Yongjun Yoon, Capt, USAF

5d. PROJECT NUMBER

5e. TASK NUMBER

5f. WORK UNIT NUMBER

7. PERFORMING ORGANIZATION NAME(S) AND ADDRESS(ES)

Air Force Institute of Technology
Graduate School of Engineering and Management (AFIT/EN)
2950 Hobson Way
WPAFB OH 45433-7765

8. PERFORMING ORGANIZATION REPORT NUMBER

AFIT-ENG-MS-18-J-009

9. SPONSORING / MONITORING AGENCY NAME(S) AND ADDRESS(ES)

Intentionally Left Blank

10. SPONSOR/MONITOR'S ACRONYM(S)

11. SPONSOR/MONITOR'S REPORT NUMBER(S)

12. DISTRIBUTION / AVAILABILITY STATEMENT

DISTRIBUTION STATEMENT A:
APPROVED FOR PUBLIC RELEASE; DISTRIBUTION UNLIMITED.

13. SUPPLEMENTARY NOTES

This material is declared a work of the U.S. Government and is not subject to copyright protection in the United States.

14. ABSTRACT

Phased arrays are essential to airborne GMTI, as they measure the spatial angle-of-arrival of the target, clutter, and interference signals. The spatial and Doppler (temporal) frequency is utilized by STAP to separate and filter out the interference from the moving target returns. Achieving acceptable airborne GMTI performance often requires fairly large arrays, but the SWAP requirements, cost and complexity considerations often result in the use of subarrays. This yields an acceptable balance between cost and performance while lowering the system's robustness to interference. This thesis proposes the use of knowledge aided adaptive radar to institute adaptive subarray nulling in concert with digital space-time adaptive processing to improve performance in the presence of substantial interference. This research expands previous work which analyzed a clutter-free AMTI application of KASPS and updates this previous research by applying the same concept to the GMTI application with clutter and STAP.

15. SUBJECT TERMS

phased array,subarray,electronic protection, adaptive nulling, knowledge-aided subarray pattern synthesis, space time adaptive processing

16. SECURITY CLASSIFICATION OF:			17. LIMITATION OF ABSTRACT	18. NUMBER OF PAGES	19a. NAME OF RESPONSIBLE PERSON
a. REPORT	b. ABSTRACT	c. THIS PAGE			Lt Col P. M. Corbell, AFIT/ENG
U	U	U	UU	70	19b. TELEPHONE NUMBER *(include area code)* (937) 255-3636, x4370; phillip.corbell@afit.edu